UiT The Arctic University of Norway

Faculty of Science and Technology

Department of Physics and Technology

Comparison of numerical wind modelling on hectometric and km scales at Kvitfjell wind power plant

Kristine Rein

EOM-3901 Master's thesis in Energy, Climate and Environment 30 SP June 2023

Abstract

Evaluating the performance of numerical weather models (NWMs) is crucial to identify the best choice of model for wind resource assessments. This thesis has investigated how well NWMs with different horizontal resolutions reproduced the wind directions, the wind speeds and the associated power production at a wind power plant located in complex terrain. The evaluated models included NORA3, WRF1km, and AROME Troms and Finnmark (ATF300m) throughout the 9 months from January to September 2022, as well as WRF111m for some case studies of shorter duration. The models were evaluated by comparing the simulations' results to hub-height wind measurements. ATF300m outperformed the other models in terms of lower errors when considering the time period as a whole, and also for a case with wind directions similar to the main wind direction registered for the park. This could be as a result of the better topographic representation by the model, thereby including terrain induced effects on the wind more accurately such as orographic blocking. However, NORA3 outperformed the other models in terms of lower errors for two cases with wind directions coming from the NW sector. These results may suggest that 3 km grid spacing gives a sufficient representation of the wind fields when the wind is coming from the open ocean and is less influenced by the terrain before entering the park. Another suggestion may be that the coarser spatial resolution of NORA3 provides lower simulated wind speeds which counteracts the overestimation related to the absence of a wind farm parameterization.

Acknowledgements

First of all, I would like to thank my supervisor Professor Yngve Birkelund for the great guidance and valuable discussions throughout this thesis. I would also like to thank my co-supervisor Associate Professor Eirik Mikal Samuelsen. Without the two of you this thesis would not have been possible to finalize.

To my fellow students. Thank you for making the years of studies a memorable time.

Lastly, I would like to thank my friends and family for the endless support I have received throughout the years. I will forever be grateful.

Table of Contents

1 Introduction

1.1 Background

Our actions this decade will heavily influence whether global warming can be limited to 1.5°C or 2°C. There is thus an urgent need to accelerate the reductions in greenhouse gas emissions within all sectors (IPCC, 2023). As of 2019, the energy supply sector accounted for 34% of greenhouse gas emissions (IPCC, 2022). Increasing the share of power generation originating from renewable energy sources while limiting the usage of fossil fuels is thus crucial towards the green transition.

Norway is today in theory self-sufficient of power and has enough installed power capacity to supply its own consumption even at hours when the power demand is high and the power production availability is low (Buvik et al., 2022). In practice however, power is occasionally being imported from abroad as power trading between nations reduces the overall costs (Olje- og energidepartementet, 2022). With the ongoing electrification of society and the increased demand for power coinciding with the moderate growth in production capacity, the Norwegian Water Resource and Energy Directorate has found that hours with national power deficit in 2030 may occur (Buvik et al., 2022). This is in line with Statnett's prognosis of a deficit in the energy balance of Norway from 2027 (Vagner et al., 2022).

Expanding the renewable power production is thus not only necessary in the mitigation of climate change but also vital to meet the increasing energy demand and ensuring a stable national power balance. When comparing electricity production from renewable energy sources, wind energy is identified as one of the most cost effective sources with large accessible potential (X. Wang et al., 2011). To identify suitable locations for wind power plants, numerical weather models (NWMs) can be used to provide wind resource assessments to give insight about the available wind conditions at a site.

1.2 Former research

Several studies have investigated how well the Weather Research and Forecasting (WRF) model reproduces the wind features in complex terrain (Carvalho et al., 2012; Fernández-González et al., 2018; Jiménez & Dudhia, 2013; Solbakken et al., 2021).

Jimenez & Dudhia (2013) investigated how well WRF at 2 km horizonal resolution reproduced the surface wind direction over complex terrain. The wind direction differences were found to decrease with increasing wind speeds. Differences between WRF and the measurements were larger in areas of complex terrain compared to flatter areas, and the 2 km horizontal resolution was concluded to not sufficiently reproduce the orographic features. The importance of choosing the most representative grid point was highlighted for some of the locations. By choosing the grid point with a topography representation close to the observational site, the wind direction differences were lowered.

Solbakken et al. (2021) evaluated how well WRF with horizontal resolutions at 27 km, 9 km, 3 km, and 1 km reproduced surface winds at Kvitfjell wind power plant. By increasing the horizontal resolution to 3 km, the errors were lowered. Although increasing the resolution further to 1 km did not improve the error, the mean wind features and wind speed variations were better reproduced. Terrain induced effects on the wind were also represented best at highest horizontal resolution as only the 1 km simulation was able to reproduce strong downslope wind.

A tendency of WRF to underestimate the occurrence of high wind speeds has been reported (Carvalho et al., 2012; Fernández-González et al., 2018). Carvalho et al. (2012) found an increase in the underestimation of wind speeds in areas with higher degree of complex terrain. By increasing the spatial resolution of the model, the simulation reproduced the terrain and the wind features more accurately. This was also found in Fernández-González et al. (2018) where increasing the spatial resolution of the model from 3 km to 1 km, increased the accuracy of the modelled wind speeds. However, the improvements by transitioning towards higher resolution cannot necessarily justify the higher computational costs (Carvalho et al., 2012).

1.3 Aim of the thesis

The purpose of this thesis is to investigate whether numerical weather models on a hectometric scale can provide further insight in the power production at Kvitfjell wind power plant when compared to numerical weather models on a km-scale. This will be achieved by studying a 9-month period of model data at different horizontal resolutions, including several cases of shorter duration. Model simulations with horizontal resolutions of 3 km, 1 km, 300 m, and 111m have been compared with the field measurements to examine the performance of each model. This

include evaluating the modelled and measured wind directions, wind speeds and the associated power and energy production.

1.4 Thesis structure

The outline of this thesis is as follows: Chapter 2 includes the theory on wind power generation and numerical weather modelling. In addition, the statistical methods used in the thesis are described. Note that some parts of this chapter are directly copied from the preliminary project paper written by the author of this thesis. Chapter 3 provides the description of the site, the data availability and the set up of all the relevant simulations. The results are presented and discussed in chapter 4 including sources of errors. Chapter 5 presents the conclusion and suggestions for future research.

2 Theory

2.1 Wind

The Sun unevenly warms the Earth resulting in the general circulation of the atmosphere. As the air at the surface is heated by the Sun, the air will rise, yielding a low pressure called thermal low at surface. This will induce a horizontal pressure difference at the same level of height generating a pressure-gradient force (PGF) acting on the air making it move and thereby causing the wind to blow. The PGF is directed normal to the lines of constant pressure, the isobars, from high pressure toward lower pressure. When air movement is initiated by the PGF, the Coriolis force (CF) will bend the track of the wind by deflecting the air to the right in the Northern Hemisphere and to the left in the Southern Hemisphere due to Earth's rotation (Ahrens & Henson, 2020).

Geostrophic air flow is an approximation of the true wind neglecting the frictional influence. In this simplified situation, the isobars are evenly spaced as straight lines. The air flow is under the influence of the PGF and the CF until the forces balance each other, resulting in a constant straight-line air flow. This constant wind blows parallel to the isobars and is called geostrophic wind. The wind speed is related to the magnitude of the PGF, and the stronger the PGF is, the stronger the wind will blow. However, the true pressure fields are more complex and the isobars are usually not straight, but curved (Ahrens & Henson, 2020).

Curved isobars yield an imbalance between the PGF and the CF acting on the air flow. This results in a gradient wind, a constant air flow following the curved isobars aloft. In the Northern Hemisphere, the air flow is counterclockwise or so-called cyclonic around a low pressure aloft, while clockwise or anticyclonic around a high aloft. Moreover, the imbalance between the PGF and CF yields higher wind speeds around a high pressure than around a low pressure for situations with the same pressure gradient present (Ahrens & Henson, 2020).

Within the planetary boundary layer, which stretches up to an altitude of around 1000 m above ground level (magl), Earth's frictional influence is present. Friction lowers the wind speed and changes the wind direction in such a way that the wind blows towards lower pressure. The presence of the terrain gives also rise to special wind effects such as mountain waves and gap winds (Ahrens & Henson, 2020).

2.1.1 Mountain waves

Mountain waves are generated under certain conditions when air flows over topography, and can result in lee waves, rotors, and downslope windstorms (Jackson et al., 2013).

Downslope windstorms can generate wind speeds down the lee side of a mountain with a magnitude 2-3 times higher than the winds at the mountain top. In order for downslope windstorms to occur the mountain must be of a certain height, and both a strong across-barrier wind and a stable atmosphere are needed at a height near the level of the mountaintop. The winds are classified into foehn winds, which are warm downslope windstorms, and bora-type winds which are cold winds (Jackson et al., 2013, p. 157).

A parameter indicating whether the air approaching a mountain will be able to flow over it is the non-dimensional mountain height $\widehat{H}$ defined as

$$\widehat{H} = \frac{NH}{U} \tag{2-1}$$

where H is the mountain height, U is the component of the wind speed orientated normal to the mountain, and N is the stability, or the Brunt Väisälä frequency. The Brunt Väisälä frequency is defined as

$$N = \sqrt{\frac{g}{\theta}\frac{d\theta}{dz}} \tag{2-2}$$

where g is the gravitational acceleration, z is the height, and θ is the potential temperature. The flow will largely be over the mountain when $\widehat{H} \leq 1$. On the the other hand, a too large $\widehat{H}$ ($\widehat{H} \gg 1$) will result in the mountain fully blocking the airflow, thereby preventing air flowing over the mountain forcing it around the mountain.

2.1.2 Gap winds

Gap winds occur in valleys and in fjords as air moves following the opening in the terrain. Strong gap winds are most frequent during winter when cold high pressures are formed inland and lower pressures are formed at sea level. This will result in a strong PGF across the mountain barrier directed towards the low pressure thereby causing air movement towards the sea. The air will follow the gaps at high speeds, yielding windstorms down the mountain (McMurdie &

Houze, 2006). The wind will accelerate on its way down and reach its highest speed at the exit of the gap (Jackson et al., 2013).

2.2 Wind-related calculations

2.2.1 Wind speed

Atmospheric motions can be described by three velocity components: the zonal (west-east) velocity component u $\left(\overset{\text{def}}{=} \frac{dx}{dt}\right)$, the meridional (north-south) velocity component v $\left(\overset{\text{def}}{=} \frac{dy}{dt}\right)$, and the vertical velocity component w $\left(\overset{\text{def}}{=} \frac{dz}{dt}\right)$. The horizontal velocity vector $\boldsymbol{V} = u\boldsymbol{i} + v\boldsymbol{j}$,where **i** and **j** are the zonal and meridional directions, respectively, is often synonymous by the term wind as the horizontal scale tends to greatly exceed the vertical (Wallace & Hobbs, 2006a). The speed of the wind is thus found by the length of the horizontal velocity vector:

$$V = \sqrt{u^2 + v^2} \tag{2-3}$$

2.2.2 Wind direction

The wind direction is defined as the direction the wind blows from and may be expressed in degrees about a 360° circle. Wind directions of 0°, 90°, 180°, and 270° correspond to a wind coming from the north, the east, the south, and the west, respectively (Ahrens & Henson, 2020). The wind direction can be found based on the horizontal wind components:[1]

$$\phi = mod\left(180 + \frac{180}{\pi} atan2(v, u), 360\right) \tag{2-4}$$

2.3 Wind power

The kinetic energy of the wind is given as

$$E_k = \frac{1}{2} m v^2 \tag{2-5}$$

where m is the air mass and v is the wind speed. As the volume flow rate through an area A is given as Av, the mass flow rate is obtained by multiplying the volume flow rate by the density ρ of the air flow

[1] ECMWF, ERA5 Q&A, https://confluence.ecmwf.int/pages/viewpage.action?pageId=133262398

$$\frac{dm}{dt} = \rho A v \tag{2-6}$$

Wind power is the time derivative of the kinetic energy and by using equation (2-5) this can be expressed as

$$P_{wind} = \frac{1}{2}\frac{dm}{dt}v^2 \tag{2-7}$$

Substituting equation (2-6) in (2-7) yields the fundamental equation for wind power

$$P_{wind} = \frac{1}{2}\rho A v^3 \tag{2-8}$$

It is evident that the power is strongly affected by the wind speed due to the cubic relation. However, all the available power in the wind cannot be converted to electricity. The power coefficient C_p defines the fraction of available power a wind turbine can extract. The power produced by the turbine is thus (Letcher & Letcher, 2017):

$$P_T = \frac{1}{2}\rho A v^3 C_p \tag{2-9}$$

C_p is limited by the Betz-limit which defines the theoretical maximum possible captured power fraction. This efficiency value is $16/27$ or near 59%.

2.3.1 Power curve

A power curve indicates the relationship between the electrical power output generated by a wind turbine and the wind speed. The cut-in wind speed is the minimal wind speed required for the wind turbine to operate, while the cut-out wind speed defines the wind speed where the turbine is programmed to stop. The wind speed where the turbine will produce maximum power output is called the rated wind speed (Wagner & Mathur, 2017). At Kvitfjell wind power plant 47 4.3 MW Siemens Gamesa wind turbines operate with a power curve deviating from the conventional power curve design and is shown in Figure 2-1 (Simonsen & Brennan, 2022). Siemens has developed the "High Wind Ride Through" application which ensures longer operating range as the turbine stepwise lowers its power production instead of shutting completely down at wind speeds exceeding 25 m/s. Siemens argues that this should reduce the fatigue, yield more operating hours and enhance the stability of energy production (Siemens Gamesa, 2018).

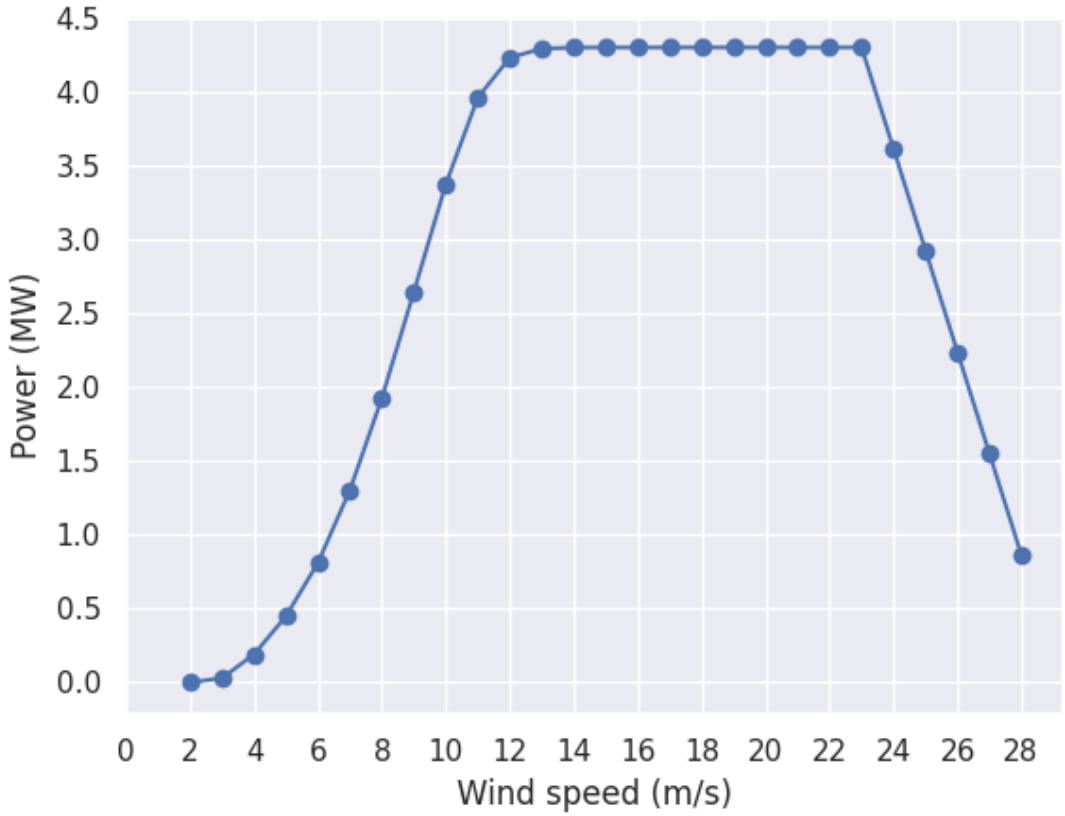

***Figure 2-1**:The power curve of a 4.3 MW Siemens Gamesa turbine (Simonsen & Brennan, 2022)*

2.3.2 Power losses

2.3.2.1 Wind turbine wakes

When comparing the air flowing upstream and downstream of a wind turbine, the wind speed decreases while the turbulence increases when the air flows through the turbine as part of the energy in the air is extracted by the turbine. The volume of the affected air flowing downstream of a turbine is called a wind turbine wake. The wake will gradually spread and return to free flow as the air progresses downwind of the turbine. Within a wind power plant, any downwind turbine will be shadowed if a wake crosses the sweeping area of the turbine. Wake effects introduces mainly two issues in wind power plants: i) reduced power production due to the reduction of wind speed and ii) increased dynamic loads on the turbine blades due to the higher turbulence levels (González-Longatt et al., 2012). Downstream turbines experiencing shadowing can introduce power losses up to 40% (Sanderse et al., 2011). For large wind power plants, wake losses account for 10-20% of the total power output (Barthelmie et al., 2008).

2.3.2.2 Icing

Wind power plants located in cold climate are vulnerable to accretion of ice on the wind turbines. A wind turbine can shut down if extreme icing occurs. This may happen when the wind force is unable to rotate the wind turbine due to changes of the blade aerodynamics. A second possibility is if any imbalances trigger the vibration alarm which stops the turbine. Lastly, the anticipated rotor torque established from measurements of the wind speed may trigger an alarm if surpassing a limit (Homola, 2011).

Ice accretion can cause a reduction in power production as a result from the change in aerodynamics properties of the blade. Based on the icing conditions at the location, the power loss range is between 0.005 to 50% of the total power output (Parent & Ilinca, 2011). Ice accretion can also lead to measurement errors from turbine instruments, overproduction, higher fatigue on wind turbine components, lifetime reductions and electrical failure. It may also serve as a safety risk as ice can be thrown from the turbine blades (Parent & Ilinca, 2011).

Anti-icing or de-icing systems, also called Ice Prevention Systems (IPS), are needed at sites where icing occurs (Battisti, 2015). Anti-icing systems protect exposed surfaces from ice formation, while de-icing systems remove previously generated ice from the surface (Homola, 2011).

2.3.2.3 Operation and maintenance

Operation and maintenance (O&M) may include testing, replacement of components and correcting errors. Two strategies are usually followed in terms of O&M. The first is the corrective maintenance strategy where the idea is to repair when failures occur. The second strategy is preventive maintenance where routinely inspections are performed, and components are replaced based on their accumulated operative time rather than their degradation state. The goal is to avoid unpredicted malfunctions (Leite et al., 2018). The O&M costs are found to represent 5% of the total investment cost for onshore wind turbines (Ren et al., 2021).

2.4 Numerical weather modelling

Weather prediction is referred to as an initial value problem where the atmospheric variables are found based on the initial state of the atmosphere and the equations for atmospheric processes and changes over time. NWMs are computer programs that solve these equations (Al-Yahyai et al., 2010). The initial conditions rely on a combination of global observations originating from radiometers, surface reports, radiosonde data, and commercial flight level data

(Wallace & Hobbs, 2006b). Processes that are not explicitly resolved by the governing equations are parameterized, such as turbulent fluxes and cloud microphysics. By data assimilation, the model combines observational data together with the latest short-range model forecast to obtain a best guess of the initial state of the atmosphere (Doyle et al., 2013).

The horizontal resolution of a model equals the lowest gap of neighboring grid points, while the vertical resolution is defined by the number of vertical layers the atmosphere is split into. Sigma-pressure levels are often used which follows the terrain near ground and follows pressure levels higher up in the atmosphere. The use of small time steps is necessary in order to maintain numerical stable conditions (Al-Yahyai et al., 2010).

NWMs can be categorized into two model types: global models covering the entire globe, and limited area models (LAMs) covering a narrowed region. LAMs are usually run at higher resolution than the global models. However, they need to be provided with boundary conditions from global models as they are covering a narrow domain. There is a distinction in whether the NWMs assume hydrostatic balance or not. Nonhydrostatic models assume an imbalance between the vertical PGF and the atmospheric weight, hence vertical acceleration and motion are accounted for. A higher demand for computational resources or longer calculation runs applies for these models (Al-Yahyai et al., 2010).

All variables are represented as finite data sets, so called discretized, either by *grid-point* methods or *series-expansion* methods. Grid-point methods define variables at grid points distributed in the domain. The solutions can further be found by *finite-difference* methods. Finite-difference methods define a solution only at the grid points, and any spatial derivatives are found by grid point differences. (Doyle et al., 2013).

The spatial resolution of the model affects how the characteristic features of the topography are represented by the model. The resolution of the terrain dataset can also limit the topographic representation. A coarse terrain dataset will not be able to sufficiently represent the topography if delivering data to a high-resolution model. The topography is usually smoothed, resulting in the mountain tops being represented lower than what they truly are. For the same reason, valleys can be completely missing or represented with a smaller elevation range from peaks to floors. This will in turn affect the ability to model orographic features such as downslope windstorms, lee waves, gap winds and convection which will not be completely resolved (Al-Yahyai et al., 2010).

NWMs can be used in wind energy resource assessments as a substitute to meteorological weather stations. Wind energy resource assessment applications require wind data covering at least one year. Wind measurements from weather stations have the disadvantage that they are costly and may not represent the whole wind park as the spatial resolution is dependent on the number of weather stations. In addition, they are rarely measuring wind at turbine hub height, they may have missing data, and must be operative for at least one year to be representable for the assessment. NWMs on the other hand are often free to download, have high resolution, offer data at every grid point for the model domain (the vertical included), and depending on the computational power, they can provide one year of data within a relatively short time (Al-Yahyai et al., 2010).

However, using NWMs come with some limitations. The model approximates the reality, and its resolution and time results in smoothing of the terrain. Physical processes are typically simplified due to lack of computational resources, or not well enough understood to be represented in the model. Uncertainties related to the initial state based on the insufficient observational coverage and frequency may affect the quality of the model output. The same applies for the boundary conditions which originate from coarser global models, and the characteristics of the surface that are generalized due to limitations in computational power (Al-Yahyai et al., 2010).

2.5 Statistical parameters

Model and observational data can be compared and analyzed by using different statistics (Willmott & Matsuura, 2005). Suppose that two sets of data are given: the simulated values by the model M_i and the observational values O_i, where $i = 1,2, \dots, n$ represents the individual element within the set of length n. The difference D_i between the modelled and observed value is thus:

$$D_i = M_i - O_i \tag{2-10}$$

To decide whether the simulated values are in average over- or underestimating, the mean bias error (MBE) can be found to:

$$MBE = \frac{1}{n}\sum_{i=1}^{n} D_i \tag{2-11}$$

An average overestimation of the model simulated values is characterized by a positive MBE, while an average underestimation is represented by a negative MBE. One should be careful when considering the bias as the magnitude of the error can be misleading due to large negative errors cancel out large positive errors.

The mean absolute error (MAE) and the round mean square error (RMSE) remove the signs of the errors between the model and the observations. The MAE and the RMSE are defined as

$$MAE = \frac{1}{n}\sum_{i=1}^{n}|D_i| \tag{2-12}$$

$$RMSE = \sqrt{\frac{1}{n}\sum_{i=1}^{n}|D_i|^2} \tag{2-13}$$

As RMSE varies with the square of the error, it is more sensitive to large errors.

When evaluating the wind direction, one must take into consideration that the wind direction is a cyclic variable varying between 0-360°. Northern wind directions of 1° and 259° are almost identical but will introduce large errors if no further measures are made before evaluating the statistics. Jiménez & Dudhia (2013) applies a definition that ensures the wind speed differences to be within the range [-180°, 180°]:

$$D_i = \begin{cases} M_i - O_i, & M_i - O_i \leq |180| \\ M_i - O_i - 360, & M_i - O_i > 180 \\ M_i - O_i + 360, & M_i - O_i < -180 \end{cases} \tag{2-14}$$

By the definition in (2-14), positive differences are acquired for modelled wind directions rotated clockwise of the measured wind directions, and negative differences are obtained when the modelled wind directions are rotated counterclockwise of the measurements (Jiménez & Dudhia, 2013). For comparisons of the modelled and observed wind directions performed in this thesis, (2-14) will be used rather than (2-10) in the calculations of the MBE, MAE, and RMSE.

3 Method

3.1 Study area

Kvitfjell wind power plant is located at Kvaløya, an island located at the coast of Northern Norway. The wind power plant consists of 47 4.3 MW Siemens Gamesa turbines (Zephyr, n.d.) with hub heights of 85 m (NVE, n.d.), yielding a total installed power of 202.1 MW. Kvitfjell is operated together with Raudfjell wind power plant, located only 3.6 km east of Kvitfjell. The power plants produce a combined energy of roughly 780 GWh each year, corresponding to the yearly power consumption of near 48 000 households (Zephyr, n.d.). The turbines within the power plant are located at heights ranging from 300 m up to 550 m. Figure 3-1 gives an overview of the terrain surrounding Kvitfjell.

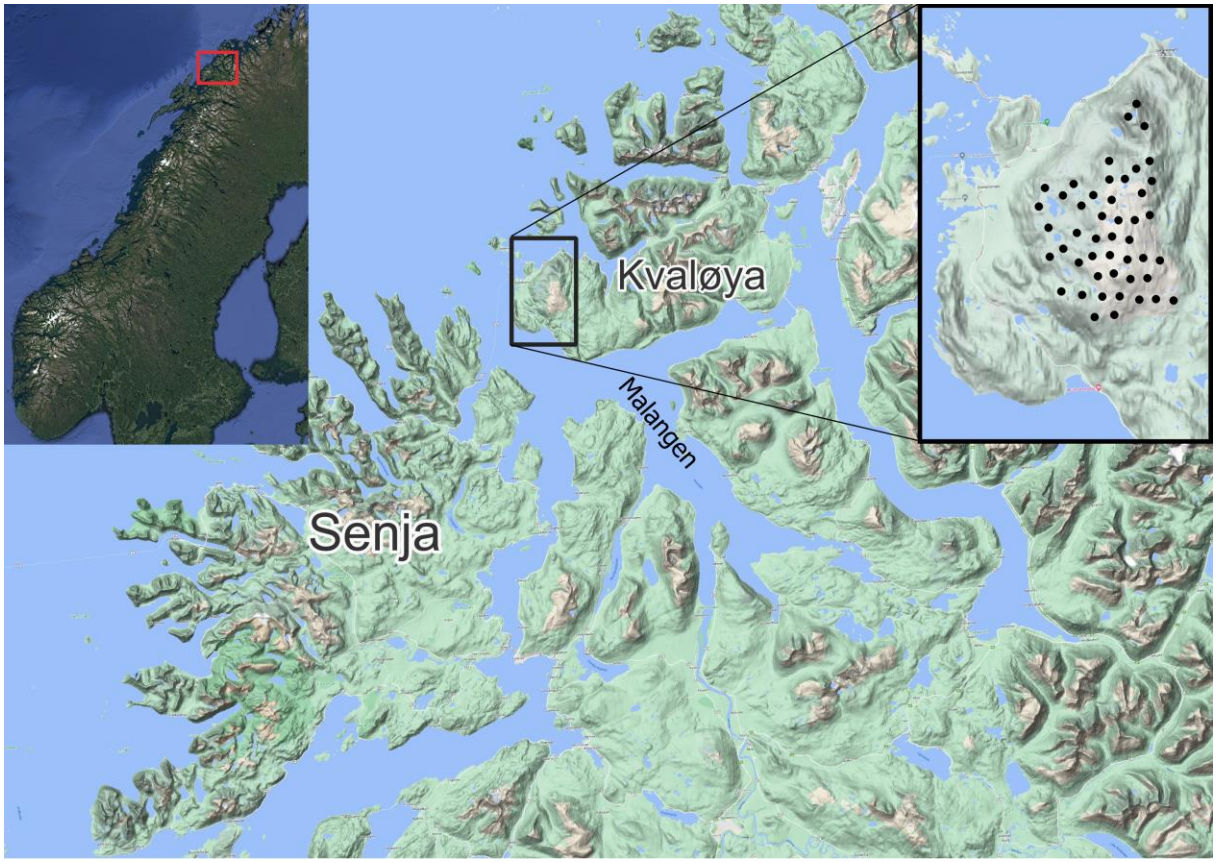

***Figure 3-1**: Overview of the terrain surrounding Kvitfjell wind power plant. Kvitfjell is located within the black square. The black dots represent the position of the wind turbines.*

The terrain in the area is complex which includes steep mountains, fjords, and islands. Southeast of Kvitfjell is the fjord Malangen which can serve as a channel for air to flow towards the power plant. Located southwest of Kvitfjell is the island Senja which include several high mountains with elevations reaching almost 1000 m. There are also mountains just above 1000 m located

northwest of Kvitfjell. Steep mountains can potentially function as orographic blockage of the wind thereby lowering the occurrence of wind coming from these directions. As Kvitfjell is located by the coast, the area northeast of Kvitfjell is open, consisting mainly of ocean except for a few small islands with elevations no higher than 200 m.

3.2 Data availability

Two different time periods were investigated: the single day of November 2nd, 2020 and the 9 months from January 1st until September 30th of 2022. The periods were chosen based on the available model simulations of AROME at 300 m horizontal resolution. The turbine measurement data was provided by Prime Capital AG. The data included measurements of the averaged wind direction, averaged wind speed, and active power recorded every 10th minute at the turbine height of 85 m.

For November 2nd, 2020 the data availability of the 10 minute sampled wind speed measurements was in total 70.1% . When investigating the wind speed measurements for each turbine, 45.8-100% of the data existed.

For the 9-month period of 2022, the numerical weather models provided hourly stored outputs. Using hourly measurements, the data availability in total was 95.7%, while the availability of the hourly data from each turbine was in the range of 86.0% to 99.4%.

3.3 Model set-up

3.3.1 WRF

The Weather Research and Forecast (WRF) model is a nonhydrostatic NWP model used for both research and forecast purposes (W. Wang et al., 2017). It can generate simulations either by initialization of an ideal case or by using real data. The latter requires output from the WRF Preprocessing System (WPS).

Before running a real case simulation with WRF, one must first prepare input data for the real program. This is done by the WPS which consists of the three programs *geogrid*, *ungrib*, and *metgrid*. Parameters for each of the three programs are specified in a common namelist file (*namelist.wps*) read by all programs. The geogrid program adds static geographical data from an external data source to the grids and thereby defines the model domains. The ungrib program collects meteorological data from external GRIB-files, and the metgrid program interpolates

horizontally the meteorological data from ungrib onto the model domain defined by geogrid. The output from metgrid is further used as input for the WRF model (W. Wang et al., 2017).

To simulate a real case, WRF uses two steps: *real.exe* and *wrf.exe*. The real program interpolates the meteorological data to the vertical levels of the model. Moreover, the boundary and initial conditions are also generated in this step. Wrf.exe yields the simulation of the model. The WRF model is controlled by a namelist file (*namelist.input)* with domain parameters equal to the ones specified in the WPS namelist file (W. Wang et al., 2017).

3.3.1.1 9 months of 2022

WRF model version 4.3 was setup with three one-way nesting domains D01, D02, and D03 as illustrated in Figure 3-2, with horizontal resolutions at 9, 3, and 1 km, respectively. The outer domain was centered at 69°58'N and 18°13'E and the inner domains were placed such that domain D02 included all extent of Lofoten, and D03 included all of Senja to resolve the nearby terrain by the highest model resolution.

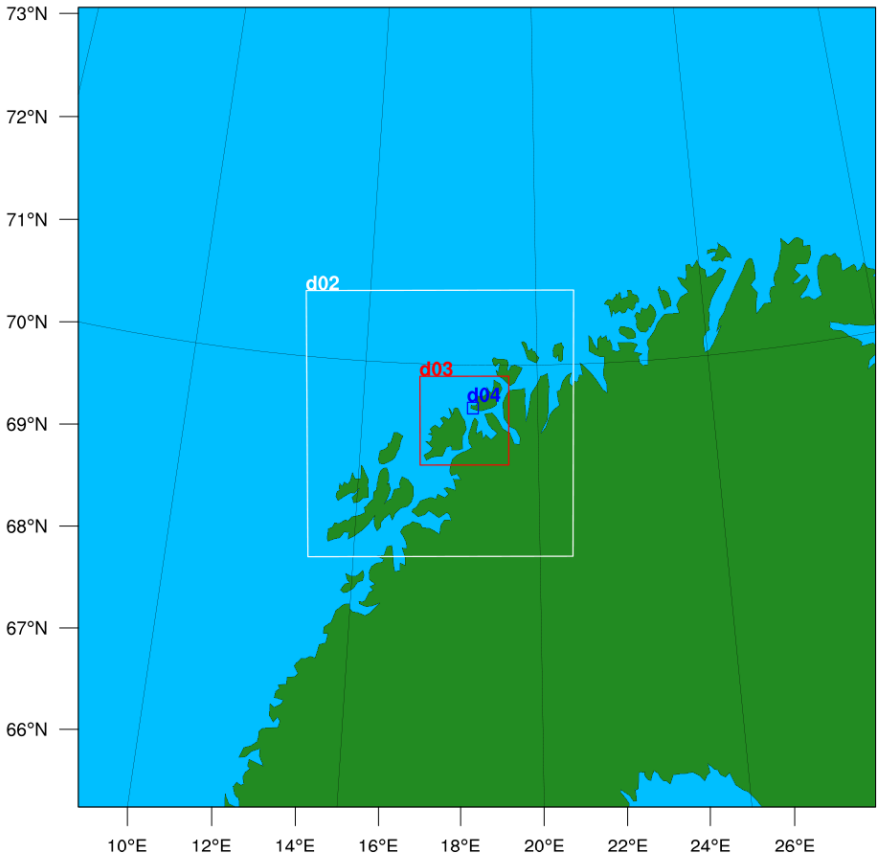

***Figure 3-2**: The domain configuration of WRF with D01 (entire map), D02 (white), D03 (red), D04 (blue).*

The terrain input data was retrieved from the Global Multi-resolution Terrain Elevation Data 2010 (GMTED 2010) with a horizontal resolution of 30 arc-seconds, corresponding to 1 km. All domains consisted vertically of 40 eta levels where the model's top level pressure was defined to 50 hPa. The initial and boundary conditions were provided by ERA5 which updated the boundary conditions hourly.

The physical processes were represented by the Thompson microphysics scheme (Thompson et al., 2008), the Mellor-Yamada Nakanishi Niino (MYNN) level 2.5 planetary boundary scheme (Nakanishi & Niino, 2009; Olson et al., 2019), the Kain-Fritsch cumulus scheme (Kain, 2004), the rapid radiative transfer model (RRTMG) shortwave and longwave radiation schemes (Mlawer et al., 1997), the unified Noah land surface model scheme (Tewari et al., 2004), the revised MM5 surface layer scheme (Jiménez et al., 2012), and the urban canopy model surface scheme (Chen et al., 2011). The physical processes are all summarized in Table 3-1.

The timesteps of the domains D01, D02, and D03 were 45 s, 15 s, and 5 s, respectively. Outputs were saved every hour. The simulations were covering the 9 months' time period from January 1st, 2022, until September 30th, 2022. The simulations were initialized 9 times, simulating one month each with 12 hours of spin up time. The 12 hours of spin up time were removed from each of the 9 simulation outputs before combining them into one netcdf file. The u and v components of the wind at the exact turbine positions were extracted at a height of 90 m by bilinear interpolation.

Table 3-1: *The chosen physical parameterization options for the WRF setup. Input options in brackets represent the options for the 111m domain.*

Variable name	Input option	Description
mp_physics	8	Thompson Scheme
ra_lw_physics	4	RRTMG Shortwave and Longwave Schemes
ra_sw_physics	4	RRTMG Shortwave and Longwave Schemes
sf_sfclay_physics	1	Revised MM5 Scheme
sf_surface_physics	2	Unified Noah Land Surface Model
bl_pbl_physics	5 [0]	Mellor–Yamada Nakanishi Niino (MYNN) Level 2.5
cu_physics	1 [0]	Kain–Fritsch Scheme
sf_urban_physics	1	Urban Canopy Model

3.3.1.2 Case November 2nd, 2020 New terrain input data

WRF model version 3.9.1 was set up with four one-way nested domains D01, D02, D03, and D04 with horizontal resolutions at 9000, 3000, 1000, and 111 m, respectively (see Figure 3-2). ERA5 provided the initial conditions and hourly updated boundary conditions. The physical processes were represented in the same way as for the 9 month period and are shown in Table 3-1. A rule of thumb is to avoid cumulus and planetary boundary layer parameterization when doing large eddy simulation. This is reflected by the [0] in Table 3-1 indicating the value for the inner domain with resolution at 111 m.

The investigated time period was the day of November 2nd, 2020. A total of three different simulations were executed. The first simulation had domains consisting vertically of 70 sigma levels with 50 hPa defining top level pressure. The static geographical data was based on the 20-category Moderate Resolution Imaging Spectroradiometer (MODIS) land use data and the Global Multi-resolution Terrain Elevation Data 2010 (GMTED 2010), both with a resolution of 30 arc-second. This corresponds to a resolution of 1 km. Both the second and the third simulation had terrain data input from a digital elevation model of 10 m resolution (DEM10). The second simulation consisted vertically of 70 levels with 50 hPa defining top level pressure, while the third simulation was set up with more vertical model levels closer to ground which were manually defined. This included a total of 79 vertical levels for the third simulation. The outputs of all simulations were saved every 10th minute. The horizontal wind components at the exact turbine positions were extracted at a height of 90 m by bilinear interpolation.

3.3.1.3 2022 cases

Three case simulations of WRF model version 3.9.1 were setup identical to the simulation with DEM10 terrain and 70 vertical levels (see 3.3.1.2). The investigated time periods were chosen based on the measurements of the wind speed and direction and consisted of the following:

- Case 1: January 13th 12:00 UTC to January 14th 08:00 UTC.
- Case 2: January 31st 19:00 UTC to February 1st 11:00 UTC.
- Case 3: May 15th 09:00 UTC to May 16th 14:00 UTC.

The first 6 hours of each simulation were discarded as spin up time. The horizontal wind components at the exact turbine positions were extracted at a height of 90 m by bilinear interpolation.

3.3.2 AROME

National Meteorological Services (NMSs) from 10 European countries are today members of the The High Resolution Limited Area Model (HIRLAM), an international research program launched in 1985. The member countries include Denmark, Estonia, Finland, Iceland, Ireland, Lithuania, the Netherlands, Norway, Spain, and Sweden, while France is an associate member. Likewise, 16 central European NMSs are today members of Aire Limitée Adaptation Dynamique Développement International (ALADIN). The ALADIN and HIRLAM agreed on developing a state-of-the-art numerical weather prediction model for both research and operational purposes accessible for all members. This led to the AROME model being adapted by the HIRLAM consortia, resulting in the HARMONIE-AROME (hereafter HA) configuration (Bengtsson et al., 2017).

HA is a nonhydrostatic operational NWP model used for short-range weather forecasts by Norway and the rest of the member countries within the HIRLAM program. It uses a semi-Lagrangian advection scheme on an A grid and a semi-Implicit two-time-level scheme. (Bengtsson et al., 2017). In order to investigate the single case on November 2nd, 2020 and the 9 month period from January to September 2022, simulations by AROME Troms and Finmark (ATF300m, Figure 3-2 left) and AROME Troms and Nordland (ATN300m, Figure 3-2 right) were further studied.

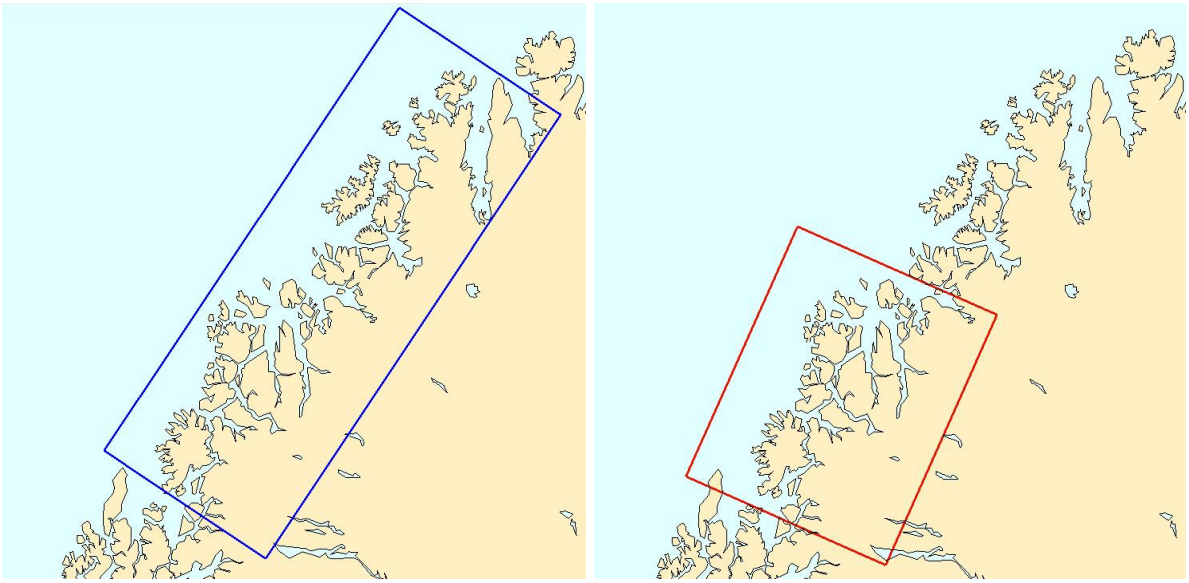

***Figure 3-3**: Domain configuration of ATF300m (blue) and ATN300m (red)*

The models were setup with HA version cycle 43h2.1 with horizontal resolutions of 300 m. The models had a time step of Δt = 5 s and consisted vertically of 90 sigma levels. The boundary conditions were provided by the European Centre for Medium-Range Weather Forecasts

Integrated Forecasting System's highest-resolution model, ECMWF IFS HRES (Owens & Hewson, 2018), which has a horizontal resolution at 9 km . ECMWF IFS HRES also provided the initial conditions for the first model run.

The model physics included the Morcrette shortwave radiation scheme from ECMWF, IFS cycle 25R1 (ECMWF, 2015), the Rapid Radiative Transfer Model (RRTM) longwave scheme (Mlawer et al., 1997), the ICE3 microphysics scheme (Lascaux et al., 2006), a semi-Lagrangian scheme for horizontal advection, a sedimentation scheme for vertical advection, a statistical cloud and condensation scheme. the HARATU turbulence scheme (Lenderink & Holtslag, 2004; van Meijgaard et al., 2012), the EDMF-M shallow convection scheme (de Rooy & Pier Siebesma, 2010; de Rooy & Siebesma, 2008; Siebesma et al., 2003; Siebesma et al., 2007)

The simulations by ATN300m were applied during the case study on November 2nd 2020. At 00 UTC, the forecast for the next 36 h was generated. The wind variables at the exact turbine locations were extracted by fimex for ATN300m at a height of 100 m.

The simulations by ATF300m were used for the 9 months study of 2022. The model provided four prognoses daily: a 12-hour prognosis at 00 UTC and 12 UTC, and a 6-hour prognosis at 06 UTC and 18 UTC. Each model run received initial conditions from the most recently prognosis, e.g., the model run initialized at 00 UTC received initial conditions from the +6h prognosis from the previous 18 UTC run. To create a continuous timeseries, the 12-hour prognoses from the 00 UTC and 12 UTC runs were merged. The analysis at the prognosis start (+0h) of each run was discarded, thus only the prognoses from +1 to +12 hours were utilized in the merging. The wind variables at the exact turbine locations were interpolated and extracted by the R-function miReadNetCDFinterpolation made by John Bjørnar Bremnes at a height of 100 m.

Outputs were saved every hour. The models were executed by Dr. Eirik Mikal Samuelsen, researcher and senior meteorologist at MET Norway.

3.3.3 NORA3

The 3-km Norwegian reanalysis dataset NORA3 was created by the Norwegian Meteorological Institute and covers the Norwegian Sea, the North Sea, the Barents Sea, and the Baltic Sea. NORA3 is as of May 21st, 2023 covering the period from 1974 until present and is continuously updated. The dataset was generated from the HA, Cy 40h1.2, which was set up with 65 vertical levels at a horizontal resolution of 3 km. The initial and boundary conditions were provided by

the global ERA5 reanalysis data from ECMWF which has hourly data for 137 vertical layers at a horizontal resolution of 31 km (Hersbach et al., 2020; Haakenstad et al., 2021). The initial conditions of each integration cycle were provided by implementing a surface analysis. The model is run without horizontal staggering (Haakenstad et al., 2021).

The physical processes are represented by the ICE3 (Lascaux et al., 2006), the OCND2 (Müller et al., 2017), and the Kogan autoconversion (Khairoutdinov & Kogan, 2000) microphysics schemes, the EDMF-M convection scheme (de Rooy & Pier Siebesma, 2010; de Rooy & Siebesma, 2008; Siebesma et al., 2003; Siebesma et al., 2007), the HARATU turbulence scheme (Lenderink & Holtslag, 2004; van Meijgaard et al., 2012), the Rapid Radiative Transfer Model (RRTM) longwave radiation scheme (Mlawer et al., 1997), and the ECMWF operational shortwave scheme (ECMWF, 1989). For further details about the model see Haakenstad et al. (2021).

The model runs four partly overlapping 9 hours forecasts per day which are initialized at 0000, 0600, 1200, and 1800 UTC. The model runs provide wind speed variables at some predefined height levels above ground, ranging from 20 m to 750 m. To create a continuous timeseries, the +4h to +9h prognosis of the wind speed variables from each model run were extracted from the exact turbine locations by fimex and merged. The horizontal velocity components were extracted from the height level at 100 m by using the netCDF4 library in Python, and wind speed and direction were found using equation (2-3) and (2-4), respectively.

4 Results and discussion

4.1 9 months study

To investigate the performance of the different models the wind speed, the energy production and the wind direction were compared with the measurements for each model.

4.1.1 Wind speed and direction

The timeseries of the wind speeds from the measurements and the model simulations are presented in Figure 4-1 for one turbine position. The turbine is located in the middle of the farm at the highest height of all turbines and is meant to illustrate how the wind varies throughout the period. Some measurements are missing, and the equivalent model data are therefore discarded, most profound during the period around March 1st. The wind speeds vary throughout the period, although higher wind speeds are found during the winter. The modelled wind speeds represented in colors are to a great extent overlapping with the measurements represented in black. This may suggest that the models are able to capture the changes in wind speeds well. However, there are times when the models are not able to reproduce the measured wind speeds which indicate that numerical weather models come with some limitations.

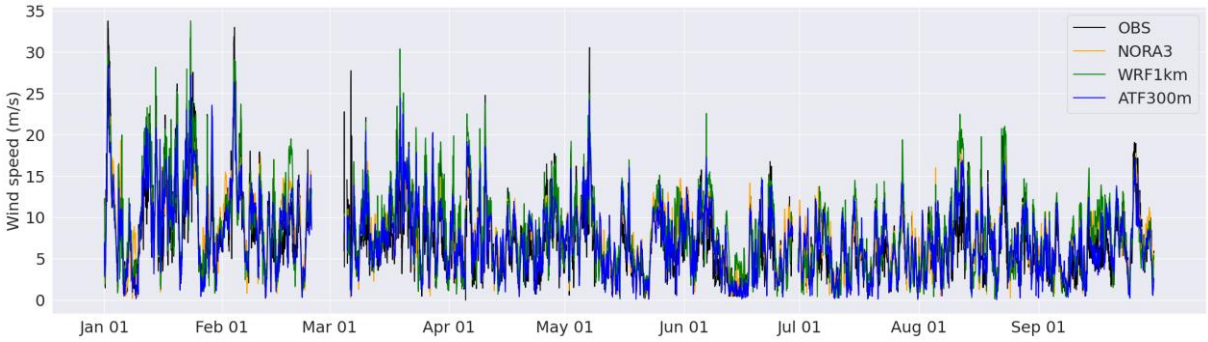

Figure 4-1: *The wind speeds from the available measurements (black, and the equivalent modelled wind speeds from NORA3 (orange), WRF1km (green) and ATF300m (blue) at turbine 12 located at the highest point in the middle of the park throughout the 9 month period.*

The distribution of the wind speeds and directions at all turbine positions is combined and represented by the wind roses in Figure 4-2. The measurements (top left) show a high occurrence of wind directions coming from S and SE. The main wind direction is SE which is occurring more than 6% of the period. Considering the terrain surrounding Kvitfjell as discussed in section 3.1, the main wind direction could be explained by the presence of the fjord Malangen located southeast of Kvitfjell. The fjord with its high surrounding mountains could serve as a channel for the air to flow from southeast towards Kvitfjell. The large portion of wind

directions coming from S could origin from the opening in the terrain located south of Kvitfjell. A portion of the measured wind directions is also coming from NW. Northwest of Kvitfjell is open ocean with a few islands of elevation no higher than 200 m. The measurements show a low occurrence of wind coming from N and SW. The latter could be a result of wind blockage from the high mountains at the island Senja.

All models fail to reproduce the low occurrence of wind coming from N, but they all simulate large occurrences of wind coming from S and SE in agreement with the measurements. NORA3 is the model that reproduces the main wind direction from SE closest to the measurements but reproduces the southerly component to a less extent than what is found from the measurements. The model fails to reproduce the low occurrence of SW wind directions. This could be related to the horizontal resolution of NORA3 being too coarse to accurately represent the heights of the mountains located at Senja, resulting in less modelled wind blocking from SW. In the sector between NE and E, the measurements indicate frequencies of winds above 2%, while NORA3 simulates the wind occurrence in this region well below 2%.

Although WRF1km (bottom left) simulates the largest occurrences of wind directions from S-SE, these frequencies are yet somewhat below of what the measurements imply. Like NORA3, the model also fails to reproduce the low occurrences of wind coming from SW, suggesting that even at 1km horizontal resolution, the degree of wind blocking from the mountains at Senja is still not accurate. The simulated wind coming from NW, NE, and E are generally in good agreement with the measurements.

ATF300m (bottom right) simulates a main wind direction coming from S which disagrees with the measurements producing a main wind direction from SE. The low occurrence of wind coming from SW is well reproduced by ATF300m which may indicate that the horizontal resolution of 300 m is needed for simulating the wind blocking from the high mountains at Senja optimally.

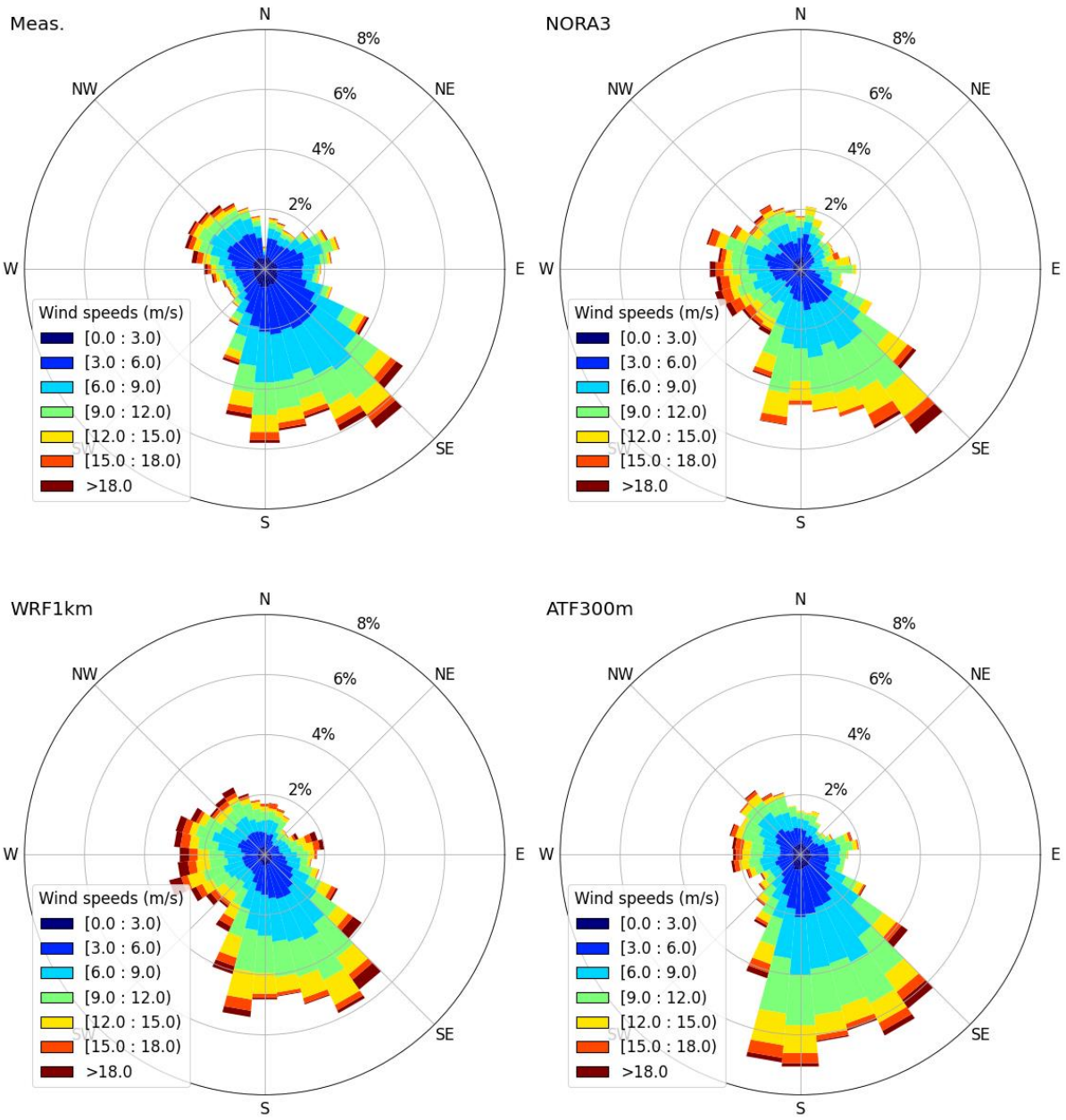

Figure 4-2: *Wind roses for all turbine positions combined. Top left: Measurements (Meas.). Top right: NORA3. Bottom left: WRF1km. Bottom right: ATF300m.*

How well the different models reproduce the different wind speeds are illustrated through histograms, presented in Figure 4-3. The figure shows the frequency of the simulated and measured wind speeds at all turbine positions. The x-axis shows the wind speed bins, while the y-axis shows the number of hours. All models are underestimating the frequency of wind speeds between 1 and 7 m/s and are therefore shifted to the right thereby overestimating the occurrence of higher wind speeds. At wind speeds between 8 and 15 m/s, the overestimation is particularly profound. ATF300m simulates the frequency of the different wind speeds closest to the

measurements for all wind speeds, except between 4 and 10 m/s. At wind speeds above 15 m/s, ATF is reproducing the occurrence of wind speeds well.

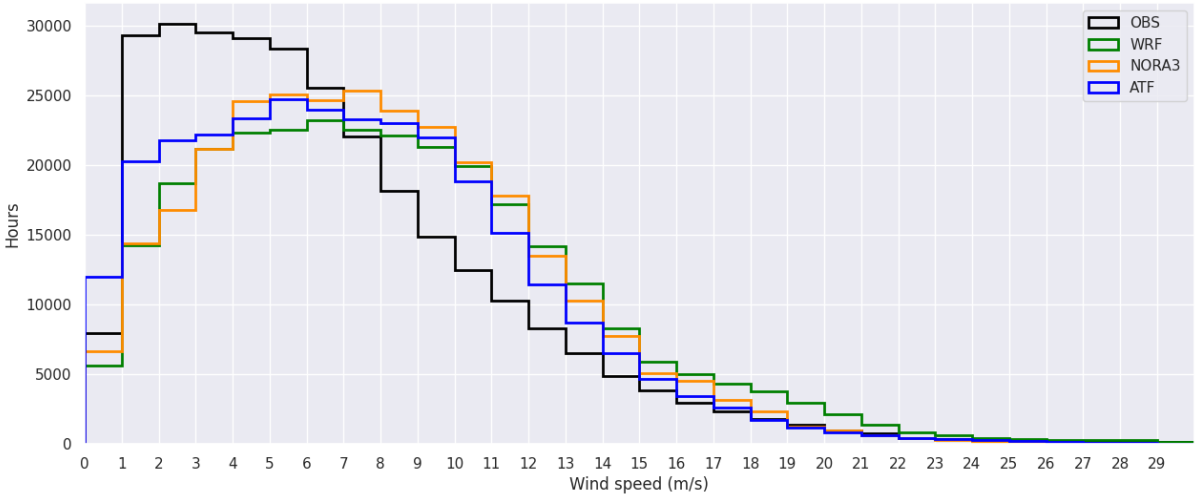

***Figure 4-3**: Combined histograms of the different wind speeds from the measurements (black), WRF1km (green), NORA3 (orange) and ATF300m (blue) for all turbine positions.*

To express how well the models simulated the wind speed, the MAE, MBE, and RMSE was found for every turbine position. Then, the averaged statistical scores were found for each model, shown in Table 4-1. All models do in average overestimate the wind speed, indicated by the positive MBE values. ATF300m has the best averaged scores of all models, with lowest values for MAE, MBE and RMSE. NORA3 scores in average as the second best model to reproduce the wind speeds, while WRF1km has the largest averaged errors of the three models. The overestimation of wind speeds is expected as none of the models take the presence of the wind turbines into consideration. Thus, wake effects contributing to the slowing down of the wind are not present in the model calculations.

***Table 4-1**:The averaged MAE, MBE, and RMSE of the wind speed of all turbine positions for the different models*

Model	MAE (m/s)	MBE (m/s)	RMSE (m/s)
NORA3	2.38	1.24	3.12
WRF1km	2.74	1.75	3.65
ATF300m	1.94	0.71	2.59

To investigate whether any spatial patterns are related to the statistical scores, the MBE of the wind speed at each turbine location is visualized for the different models in Figure 4-4. When comparing the three panels in the figure, it is evident that ATF300m (right) is the model with the overall lowest MBE, in accordance with the low, averaged MBE value. At four turbine positions located southwest, the white fields of MBE for ATF300m gives the impression that the model reproduces the wind speeds close to the measurements. This is however not certain as periods of large underestimation could cancel out periods of large overestimation and the averaged bias must thus be interpreted with caution. ATF300m overestimates the wind speeds at all other turbine positions, except for one tubine position located north where the model is slightly underestimating. The most prominent overestimation occurs at turbine positions located in the middle of the farm at the highest heights, although this is not applicable for the single turbine position located at the highest point within the farm. NORA3 (left) shows a tendency of overestimating the most for turbine positions located southeast. The overestimating gradually reduces for turbine positions located further north and west. At one of the turbine positions located the furthest west, NORA3's lowest MBE is found. WRF1km (middle) overestimates the wind speed at all turbine positions, most prominent at southern and middle positions.

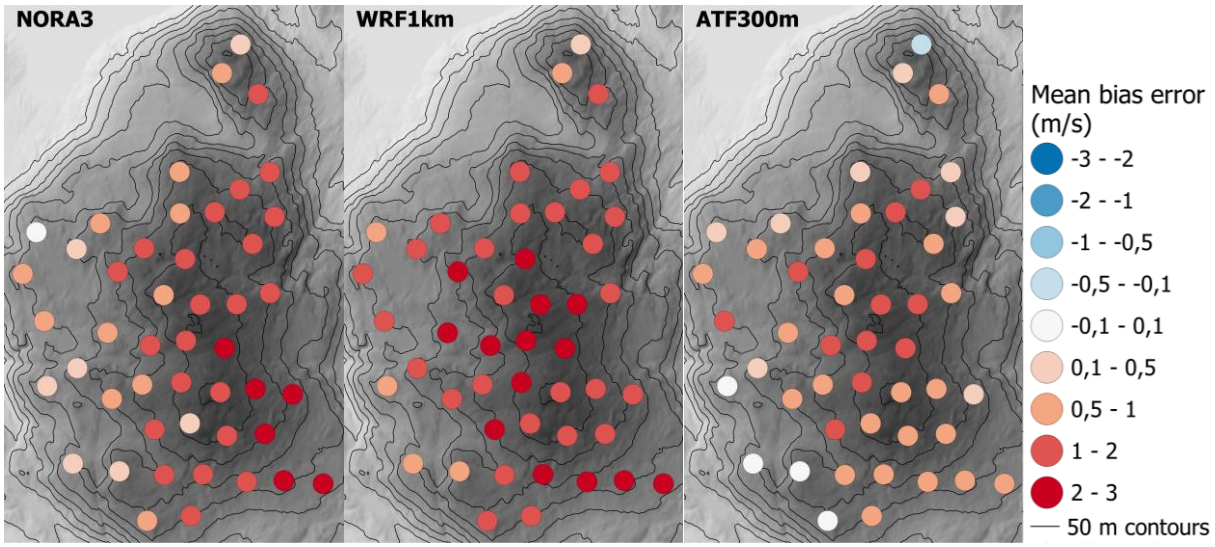

***Figure 4-4**:The averaged wind speed bias at each turbine location for NORA (left), WRF1km (middle), and ATF300m (right).*

When evaluating the spatial distribution of MAE in Figure 4-5, ATF300m (right) still stands out as the model reproducing the wind speed the best in accordance with its low averaged MAE value. It is clear that the lowest values of MBE for ATF300m from Figure 4-4 are not corresponding in position with the lowest MAE values from Figure 4-5. This is evident for the four turbine positions southwest in the park where the lowest MBEs are found, while MAEs up

to 2 m/s are found, highlighting that a low value of the MBE is ambiguous. The most prominent errors of ATF300m are located from the middle of the farm and towards north. For NORA3 (left), the largest errors are still located southeast in the park, in accordance with the locations of the largest MBE values. WRF1km (middle) appears to be the weakest model, in agreement with the large averaged MAE, MBE and RMSE values. The largest errors are located in the middle of the farm.

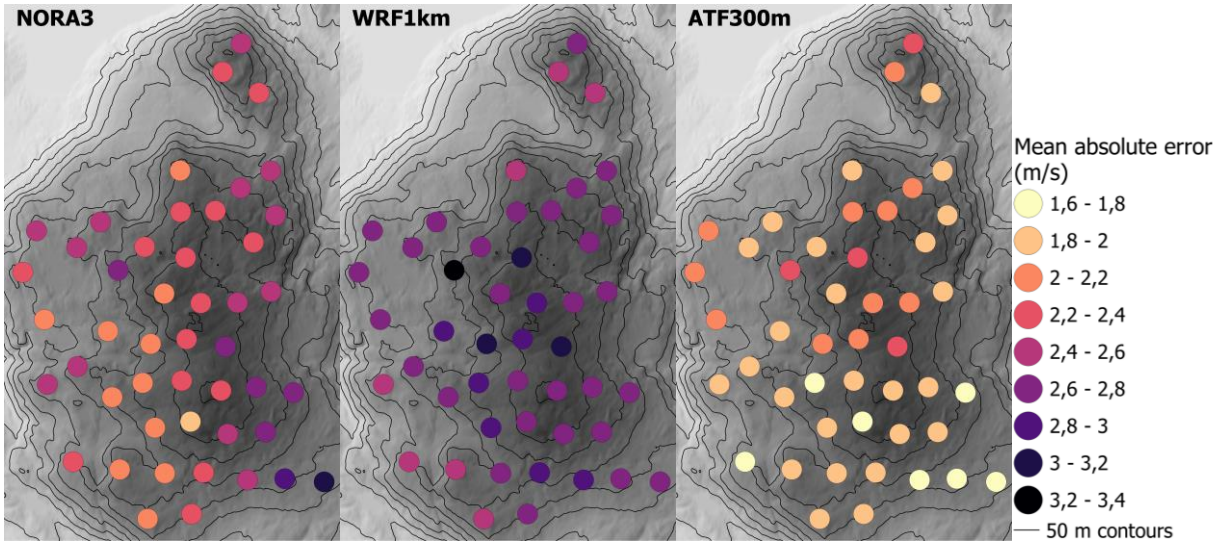

***Figure 4-5**: The spatial distribution of the MAEs of the wind speeds for NORA3 (left), WRF1km (middle) and ATF300m (right).*

The MAE, MBE, and RMSE of the wind direction at every turbine position were found for each model as given by (2-14). Then, the average scores for each model were found, shown in Table 4-2. All models do in average overestimate the wind direction. ATF300m is the model which in average simulates the wind direction closest to the measurements.

***Table 4-2**: The averaged MAE, MBE, and RMSE of the wind direction of all turbine positions for the different models.*

Model	MAE (degrees)	MBE (degrees)	RMSE (degrees)
NORA3	38.07	19.83	50.28
WRF1km	39.98	21.97	51.69
ATF300m	34.53	15.71	46.79

4.1.2 Energy production

4.1.2.1 Measured power vs measured wind speeds through power curve

The wind speed and hence the power production fluctuates with time, but they are not necessarily correlated as it from time to time can be a large difference between the measured and the calculated power. This is illustrated in Figure 4-6 which shows the timeseries of the measured power and the calculated power from the measured wind speeds at a turbine position. The founds here are similar at all the turbines. During mid-March, highlighted by the red circle, there is a clear difference between the two power measures.

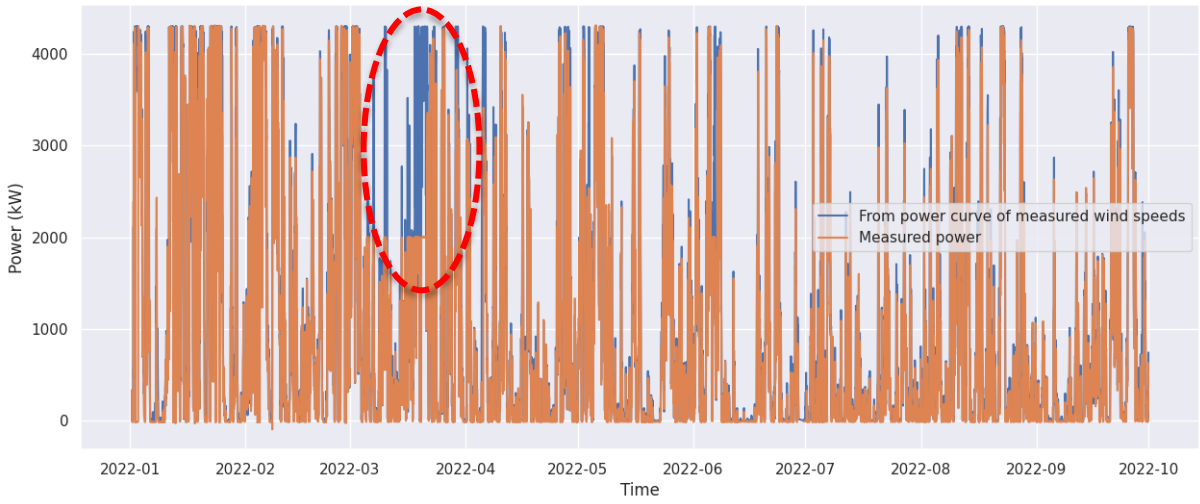

Figure 4-6: *The timeseries of the measured power and the power found from the measured wind speeds at turbine 50.*

Figure 4-7 shows a more detailed timeseries of the power production during this period. It is clear that the measured power reaches a pre-defined upper limit in power production well below of what is expected based on the wind speed measurements. This can be explained by maintenance, testing, icing or other events causing the operational power production being limited. Such events are beyond the scope of NWMs, suggesting that finding the power based on the wind speed measurements might be better suited for model verification. Another procedure would be to get an overview of all alarm logs and events registered for all turbines within the park and then exclude the affected data as also the wind measurements will likely be affected occasionally. However, due to the time limitations of this thesis, only the former option was used. The measured power data presented further in this thesis is therefore not directly from the power measurements but found from the wind speed measurements. By using the power curve from section 2.3.1, the power production associated with the measured wind speed is found.

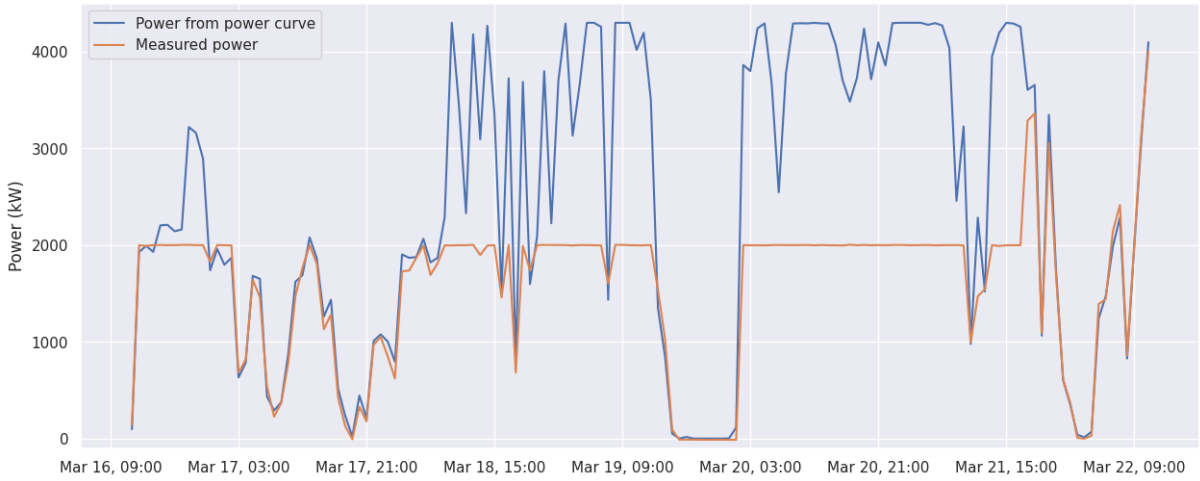

Figure 4-7: *A closer look on the measured power and the power found from the measured wind speed during mid-March at turbine 50.*

4.1.2.2 Performance of the models

The total energy production found from the measured and modelled wind speeds at each turbine position over the 9 months study is represented in Figure 4-8. From the figure it is clear that all models overestimate the energy production for each turbine position. This can be seen as a result of the overestimation of wind speeds as discussed in 4.1.1. ATF300m lies closer to the measurements for almost all turbine positions which is in line with ATF300m being the model reproducing the wind speeds closest to the measurements. All models are simulating differences within the park which is clear from the variations in energy production also found in the measurements. For instance, the models reproduce a drop in the energy production at turbine 5 and a higher energy production at turbine 6. However, there are locations where the models are not capturing the trends seen in the measurements. Like for the turbine numbers from 35 up to 38 where all models simulate the opposite of the measurements in terms of which turbines experience higher and lower productions.

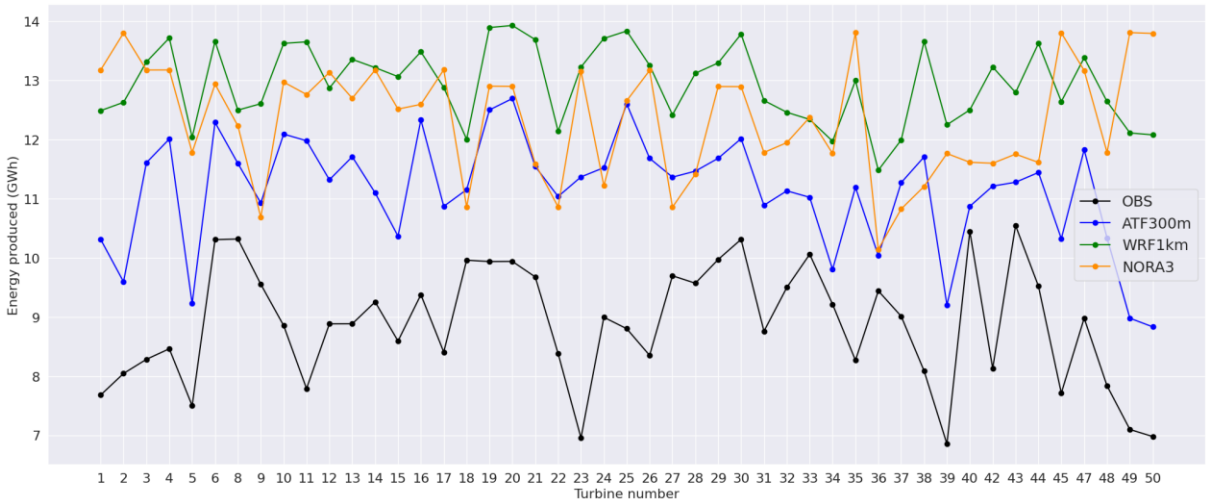

***Figure 4-8**: The total energy production at each turbine found from the wind speed measurements (black) and from the modelled wind speeds for ATF300m (blue), WRF1km (green) and NORA3 (orange).*

To express how well the models simulate the power production, the MAE, MBE, and RMSE of the power production were found for every turbine position. Then, the averaged statistical scores were found for each model, shown in Table 4-3. Just as for the wind speeds, the models are also overestimating the power production, with ATF300m standing out as the model with the lowest averaged errors.

***Table 4-3:** The averaged MAE, MBE, and RMSE of the power production of all turbine positions for the different models. The modelled and measured power productions were found by forcing the simulated and measured wind speeds through the power curve.*

Model	MAE (kW)	MBE (kW)	RMSE (kW)
NORA3	829.10	549.33	1264.99
WRF1km	930.97	646.99	1412.09
ATF300m	655.36	360.69	1044.46

The histograms of the simulated and measured energy production at different wind speeds during the first 9 months of 2022 are shown in Figure 4-9. The x-axis shows the wind speed bins, while the y-axis shows the energy produced in GWh. It is clear that all models are overestimating the energy production at wind speeds between 7 and 18 m/s, most profound between 8 and 15 m/s. This is in agreement with the positive power bias found for all models as well as the overestimation of the equivalent wind speeds found in section 4.1.1. Also worth

noting is that the underestimation of wind speeds below 7 m/s is not affecting the energy production to any extent. This is related to the power curve, where wind speeds below 7 m/s yield low to moderate power production, whereas the power production changes more rapidly at wind speeds above 7 m/s. ATF300m reproduces the energy production well at wind speeds above 16 m/s, while both NORA3 and WRF1km still overestimate.

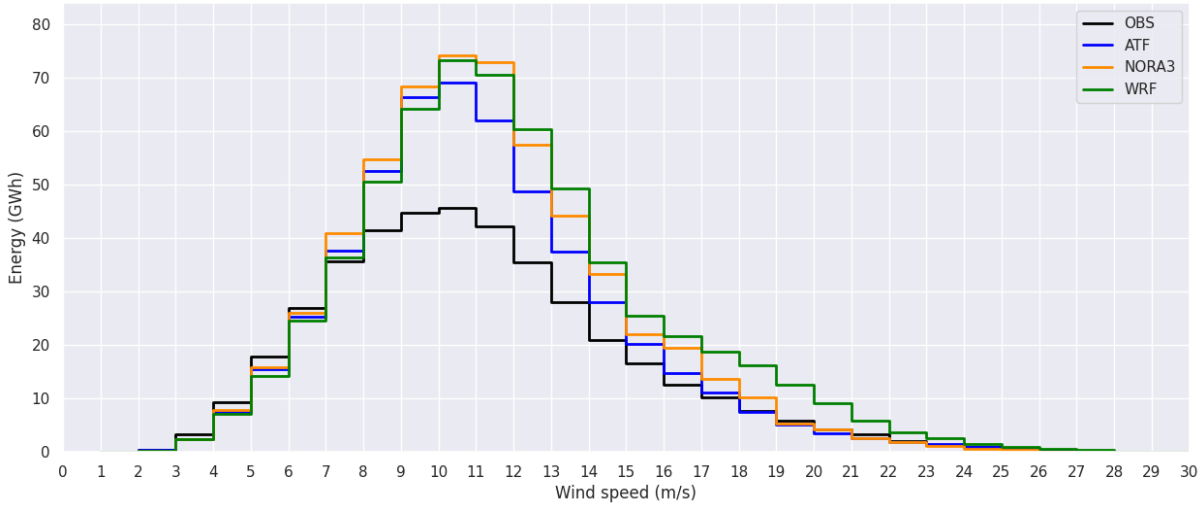

***Figure 4-9**: Histograms of the combined energy production of all turbines for the measurements (black), ATF300m (blue), NORA3 (orange) and WRF1km (green). The energy production is found from the measured and simulated wind speeds in combination with the power curve.*

Energy histograms of the type in Figure 4-9 were also created for each turbine position. The MAE, MBE, and RMSE were then found based on the energy deviation found for each wind speed bin. Only the result for the MBE is shown here in Figure 4-10, as similar results were found for the MAE and the RMSE. The x-axis shows the turbine numbers representing the different turbine positions. The y-axis shows the averaged energy error in MWh. All models overestimate the energy production at every turbine position as shown in Figure 4-10. This is as expected as all models had positive biases of the simulated wind speeds as discussed in 4.1.1. ATF300m stands out as the model with the lowest bias at all but eight turbine positions where NORA3 is somewhat better. It is evident that WRF1km has the largest offset at almost all turbine positions. Both ATF300m and WRF1km have their highest bias at turbine K23, while NORA3 has its highest bias at turbine K50.

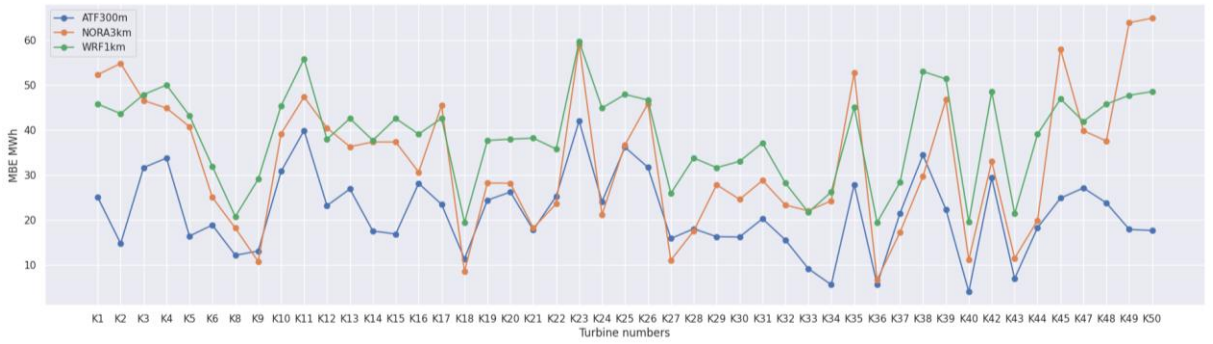

***Figure 4-10**: The MBE of the energy histograms for all turbine positions for ATF300m (blue), NORA3 (orange), and WRF1km (green). Note that the bias found is the deviation in energy produced within each wind speed bin and is thus not considering the timing of each model.*

4.2 Case study 02.11.2020

4.2.1 Terrain

Features of the terrain are better resolved with the input data at 10 m horizontal resolution compared to the input data with horizontal resolution at 1 km. This is evident in Figure 4-11 where the 1 km based input (bottom right) has much smoother transitions compared to the 10 m based terrain (bottom left).

The elevated plateau around 69.62°N, 18.15°E which ranges up to a true height of 450 masl has a height up to 439 m in the 10 m based model, while not present in the 1 km based model. The highest point at Kvitfjell is at a true elevation of 563 m, while the highest point found in the 10 m and 1 km based models are 556 m and 536 m, respectively.

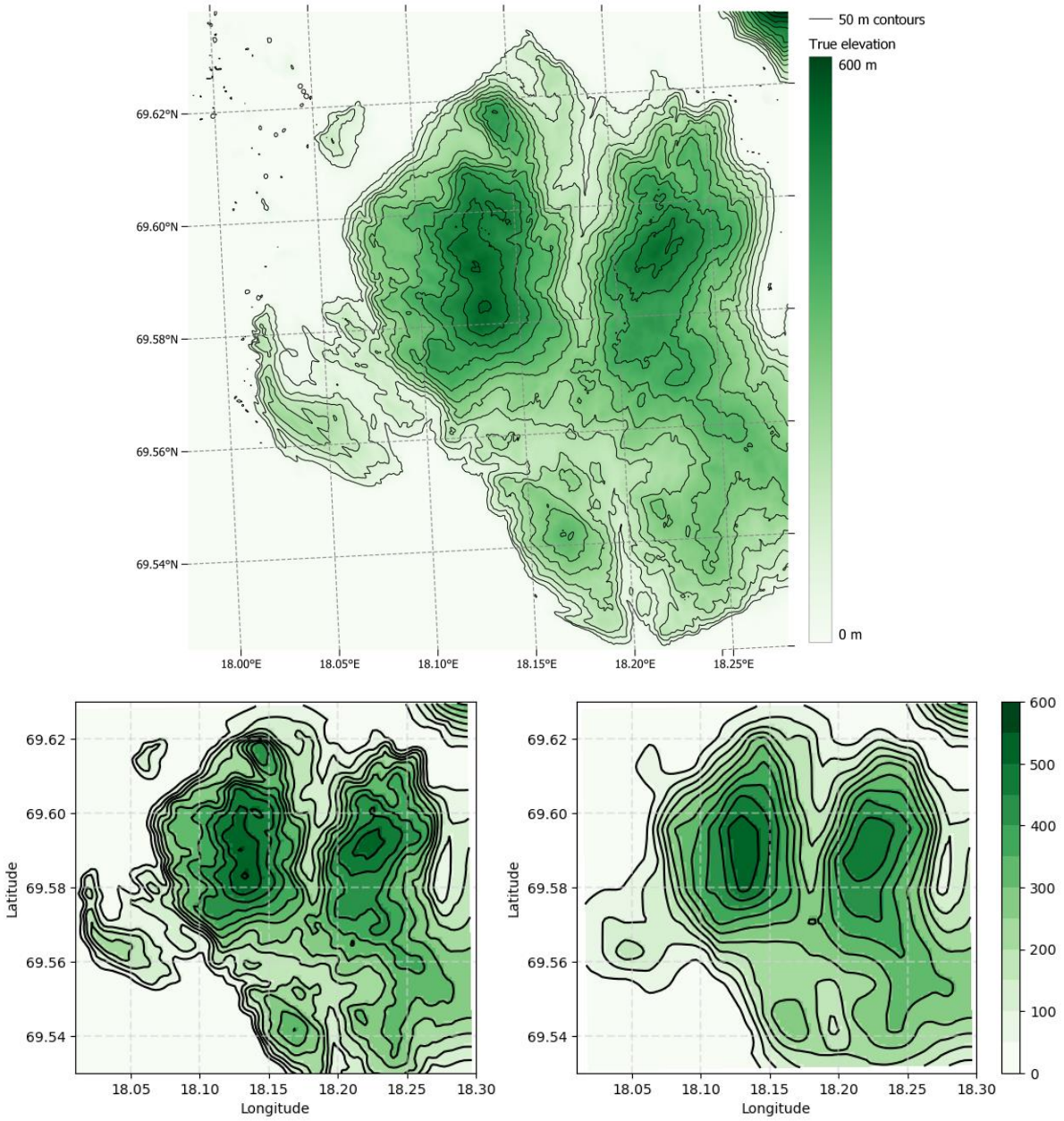

Figure 4-11: *Top: Terrain map with a 10 m horizontal resolution[2]. Bottom left: WRF111m, input data with horizontal resolution at 10 m. Bottom right: WRF111m, input data with horizontal resolution at 1 km. The black lines are 50 m contours.*

4.2.2 Wind speed deviations

The MAE, MBE, and RMSE of the wind speeds were found for each turbine position for each model configuration. Then, a spatial average over the park was performed which is presented in Table 4-4. All WRF models overestimate the wind speeds, evident from the positive MBE

[2] Terrain data downloaded from Kartverket at https://hoydedata.no/LaserInnsyn2/

values. WRF DEM10m+79η overestimates the most. Both MAE and RMSE increase as the horizontal resolution of the terrain input increases and when the vertical resolution near ground increases. This could be explained by the better terrain representation by the models with higher resolution of the terrain input data. As more features from the terrain are resolved, the wind will also be more affected by the terrain.

Table 4-4: *The models' spatial averaged MAE, MBE, and RMSE of the wind speeds.*

Model	MAE (m/s)	MBE (m/s)	RMSE (m/s)	Datapoints
WRF GMTED	1.94	0.70	2.43	4227
WRF DEM10m	2.06	1.11	2.59	4227
WRF DEM10m+79η	2.25	1.53	4.33	4227
ATN300m	2.30	-1.38	4.50	774

The spatial distribution of the MAE of the wind speeds are shown in Figure 4-12. It is clear that the wind speeds are reproduced closest to the measurements for most locations for WRF111m having GMTED as terrain input data (top left). The largest MAEs for this model configuration are found at locations near the heights in the middle of the park and at the height northeast in the park. This could be related to the incomplete representation of the terrain, although this is not certain as the largest MAEs are found at the same locations for WRF111m DEM10 and DEM10+79η.

By applying the DEM at 10 m resolution (top right) and combining it with an increase of the vertical levels (bottom left) for WRF111m, the magnitude of the MAE increases in general. ATN300m has four MAEs exceeding 4 m/s located south in the park. This could explain why ATN300m comes out worst in terms of the spatial averaged MAE of 2.30 m/s.

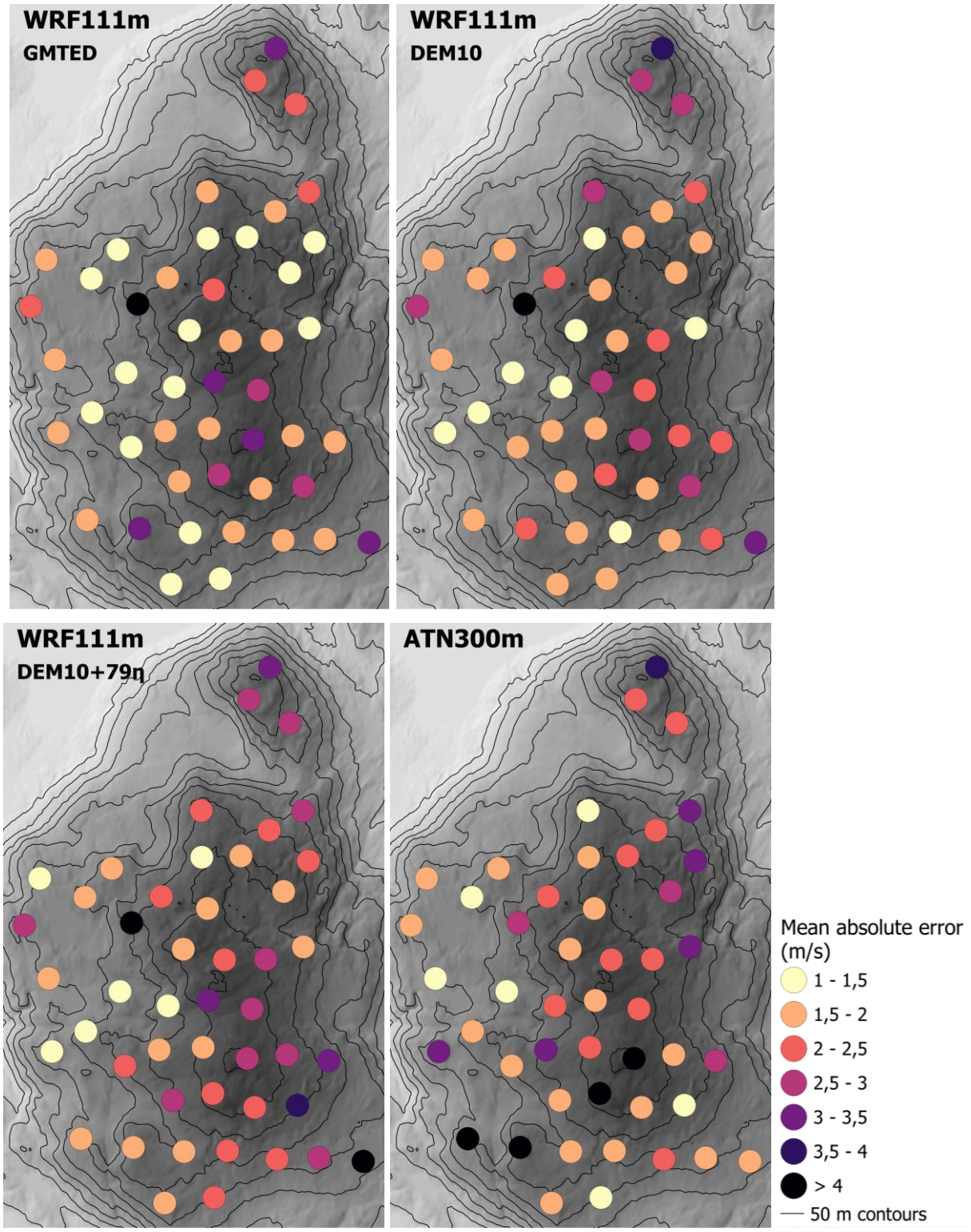

Figure 4-12: *The MAE of the wind speeds at each turbine location for WRF111m with GMTED as terrain input (upper left), WRF111m with a DEM at 10 m resolution as terrain input (upper right), WRF111m with DEM10m and 79 eta (η) levels (bottom left) and ATN300m (bottom right).*

4.3 Case studies of 2022

Three cases: January 2022, February 2022 and May 2022, were further studied. The cases were chosen based on the measurements of the main wind direction and the wind speed. The criteria for choosing a case were measurements of constant wind directions throughout the period, and wind speeds between 6 and 12 m/s. This wind speed range represents the area of the power curve where the power rapidly changes. Thus, the power production is highly sensitive to small changes in wind speed within this wind speed range. Investigating different NWMs during such conditions might give an impression of which model is best suited for power production planning.

4.3.1 Terrain representation

WRF111m, ATF300m, WRF1km, and NORA3 have different horizontal resolutions and are therefore representing the terrain differently. For illustrative purposes, Figure 4-13 shows the closeup terrain map of Kvitfjell (top), and the modelled terrain by WRF111m (middle left), ATN300m (middle right), WRF1km (bottom left) and WRF3km (bottom right). It is clear that the topography is best resolved in WRF111m and as the horizontal resolution decreases, the terrain gets more smoothed. For instance, the two heights above 550 m at the top of Kvitfjell, located around 69.59°N, 18.13°E are resolved in WRF111m, but not present in any of the other models. The heights located north around 69.62°N, 18.15°E, west around 69.56°N, 18.05°E, and southeast around 69.54°N, 18.17°E are present in both WRF111m and ATN300m, but are completely missing in WRF1km and WRF3km. The 50 m contours have a more realistic shape in WRF111m where they are curving and bending, whereas in ATN300m, WRF1km and WRF3km the contours follow a more smooth path.

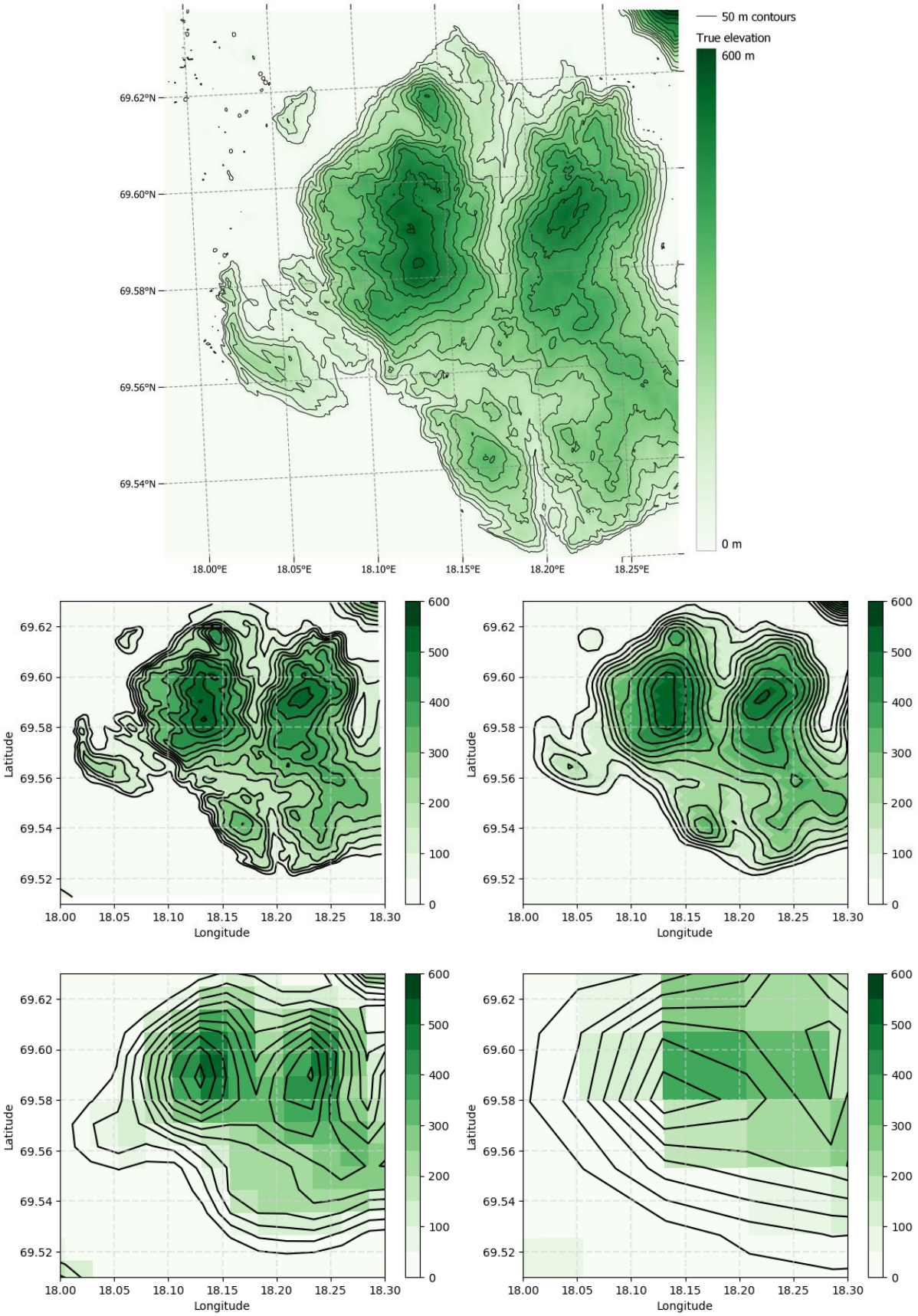

***Figure 4-13**: Terrain maps with 50 m contour lines. The different shades of green indicate the elevation in meters. Top: Map of the terrain at 10 m resolution. Middle left: Modelled terrain by WRF111m. Middle right: Modelled terrain by ATN300m. Bottom left: Modelled terrain by WRF1km. Bottom right: Modelled terrain by WRF3km.*

4.3.2 January 2022

The wind measurements from all 47 turbines within the park from January 13th 18:00 UTC to January 14th 08:00 UTC are represented by the wind rose in Figure 4-14. The main wind direction during this period was in the range of 270°-315° (W-NW). Such a wind direction implies that the wind is coming mainly from the open ocean. The wind speed was between 6 and 15 m/s, with largest occurrences of winds in the range 9 to 12 m/s. This is indeed a wind speed range where the power production will vary a lot based on the wind conditions.

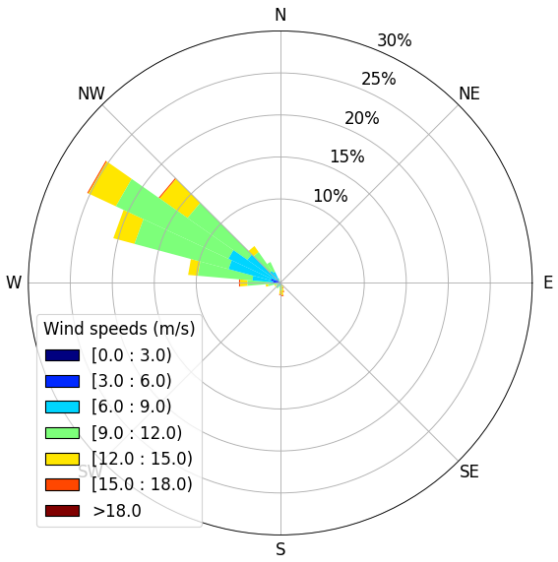

***Figure 4-14**: Wind rose of the combined hourly wind measurements from all 47 turbines from January 13th 18:00 UTC to January 14th 08:00 UTC.*

Figure 4-15 shows the sample space between the 10th and the 90th percentile of the wind speeds for the turbine measurements and the model simulations. The grey area represents the sample space of the measurements, while the whiskers represent the sample space of the different models. Each dot represents the median. It is evident that ATF300m has the largest spread in wind speeds of all models, especially until Jan 13, 23:00 UTC. The model clearly underestimates the wind speeds as the median of ATF300m is lower than the measurements at all hours, except at Jan 14, 05:00 UTC. The sample space of NORA3 is quite narrow, suggesting low variance of the wind speeds. This can be explained by the few individual locations represented by the model, as NORA3 is only able to represent the 47 turbine positions as 4 different locations. WRF111m clearly overestimates the wind speed as all its medians are well above the measurements, except at Jan 14, 07:00 UTC. WRF1km do also overestimate at most hours, in particular at Jan 13, 19:00 UTC. The hourly variance of the wind speed measurements over the period was highest at the simulation start and second highest at Jan 13, 22:00 UTC. To

investigate how well the models simulated the wind speed differences within the park, the latter time was studied further ensuring sufficient spin up time and stable conditions for WRF111m.

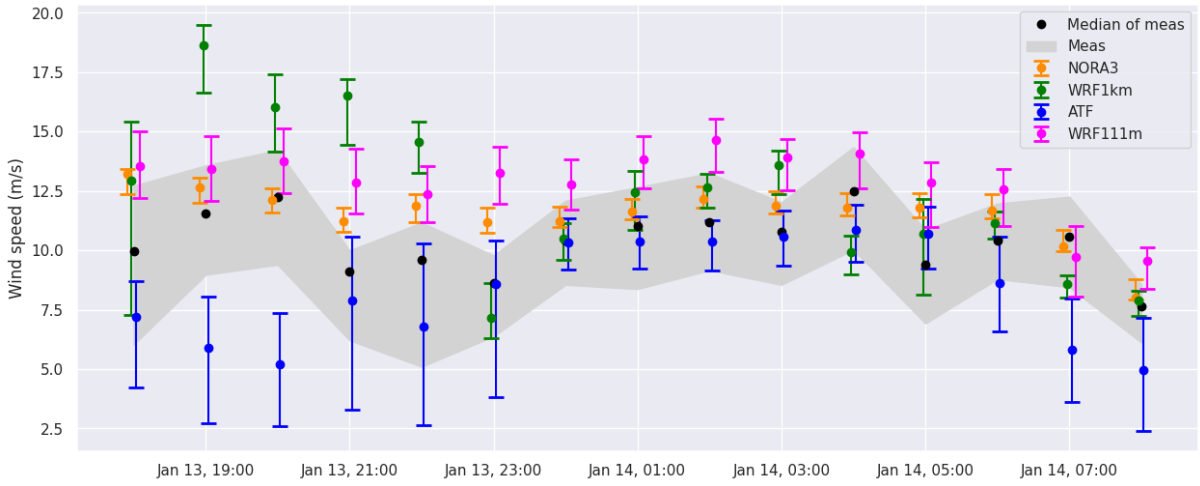

***Figure 4-15**:The sample space between the 10th and the 90th percentile of the winds speeds from the measurements (grey), NORA3 (orange), WRF1km (green), ATF300m (blue) and WRF111m (pink). The dots represent the medians.*

The MAE, MBE, and RMSE of the wind speed were found for each turbine location during the investigated period. The error of each model was then found by averaging the scores, shown in Table 4-5. NORA3 has the lowest MAE, MBE and RMSE of all models, whereas WRF1km has the highest MAE and RMSE.

***Table 4-5**: The averaged MAE, MBE and RMSE of the wind speed of all turbine positions for each model*

Model	MAE	MBE	RMSE
NORA3	1.96	1.36	2.31
WRF1km	3.13	1.92	3.93
ATF300m	2.73	-2.02	3.39
WRF111m	2.90	2.66	3.24

To investigate if there are any spatial patterns related to the model's biases, the power derived from the measured wind speeds and the models power biases at each turbine on January 13th 22:00 UTC were plotted in Figure 4-16. At each turbine location, the power found from the measured wind speed is represented by a diamond. The darker the color of the diamond is, the higher is the power production. Also highlighted at each turbine location is the bias of the model of interest. The bias is represented by a colored circle, where blue and red colors indicate under-

and overestimation, respectively. The strength of the color indicates the bias magnitude. The spatial averaged absolute error at this specific time is shown as the MAE in the upper left corner of each panel.

From Figure 4-16 it is clear that ATF300m is the model that in average underestimates the power production within the park, while NORA3, WRF1km and WRF111m predominantly overestimate. This is as expected based on the distribution of measured and modelled wind speeds from Figure 4-15. Based on the wind speed measurements, the turbines located southeast in the park yield the lowest power production represented by the white diamonds, and are the locations where NORA3, WRF1km, and WRF111m have their highest biases. As the wind is coming from NW, these positions are in the downwind area which could have been affected by the turbine wakes generated when the wind blows through the turbines located further ahead. Moreover, as these models tend to overestimate the power production, the models' biases are amplified where the measured wind speed and hence the power production is lower. This situation is flipped for ATF300m as the model's lowest biases are found in this specific area. The MAE value of ATF300m is the lowest of the four models. There are few differences between NORA3, WRF1km and WRF111m, but WRF1km overestimates somewhat more than the other two, resulting in its higher MAE.

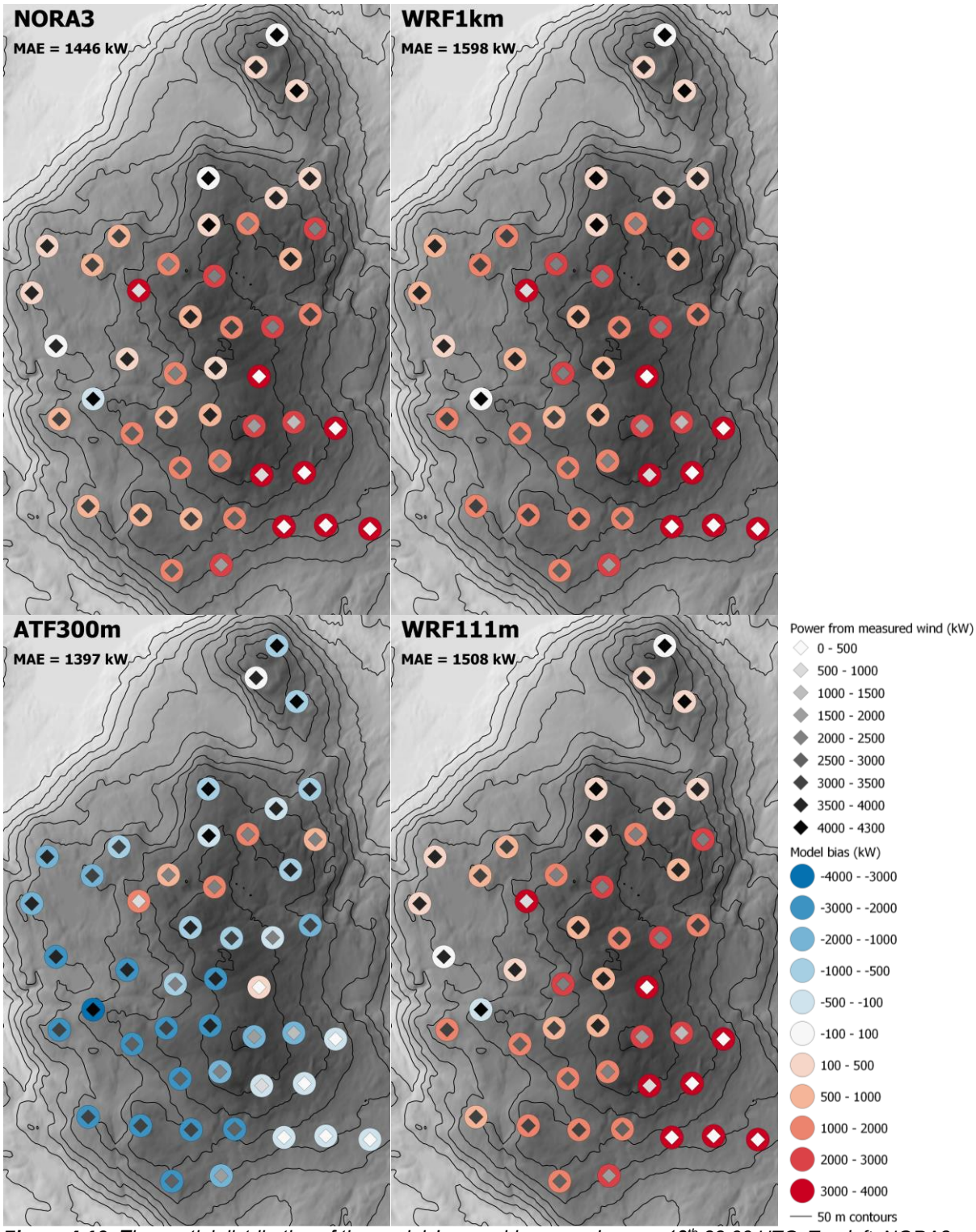

Figure 4-16: *The spatial distribution of the models' power biases on January 13th 22:00 UTC. Top left: NORA3. Top right: WRF1km. Bottom left: ATF300m. Bottom right: WRF111m.*

4.3.3 February 2022

At February 1st, from 01:00 to 11:00 UTC, the main wind direction is between 135°-180°(SE-S) as shown by the wind rose representing the turbine measurements throughout the period in Figure 4-17. This is the same direction which is measured most frequently during the 9 month period, studied in section 4.1. As there are several mountains surrounding the fjord Malangen

located southeast of Kvitfjell (see Figure 3-1), these mountains may block the wind coming from further inland, resulting in the wind being channeled through Malangen towards Kvitfjell. The majority of the measured wind speeds are in the range of 6 to 12 m/s where small changes in wind speeds heavily influences the power production.

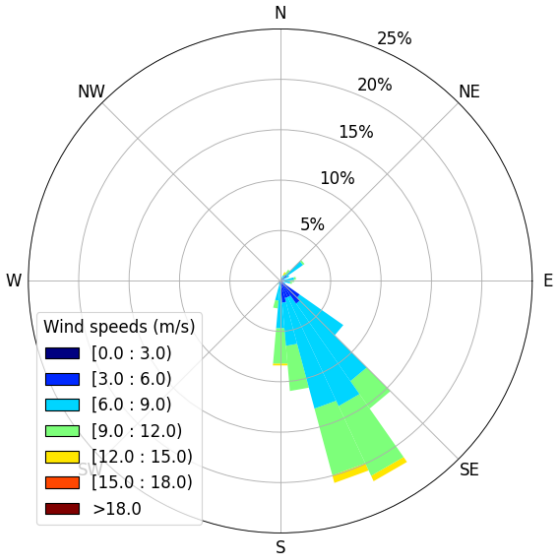

Figure 4-17: *The wind rose representing the combined hourly measurements of the wind from all 47 turbines on February 1st, from 01:00 to 11:00 UTC*

The timeseries of the measured and simulated wind speeds between the 10th and the 90th percentile are shown in Figure 4-18. At most hours, all models overestimate the wind speeds. WRF111m overestimates the wind speeds every hour. NORA3 overestimates the wind speeds from 02:00 UTC, and WRF1km overestimates the wind speed every hour except for 07:00 UTC. ATF300m overestimates the wind speeds from 06:00 UTC. The sample spaces of all models are mostly within the sample space of the measurements, although there are times when the simulated wind speeds exceed the 90th percentile of the measurements. The most prominent examples of this are WRF1km during the first four hours of simulation, WRF111m during the mid-part of the simulation and NORA3 during the last hours of simulation.

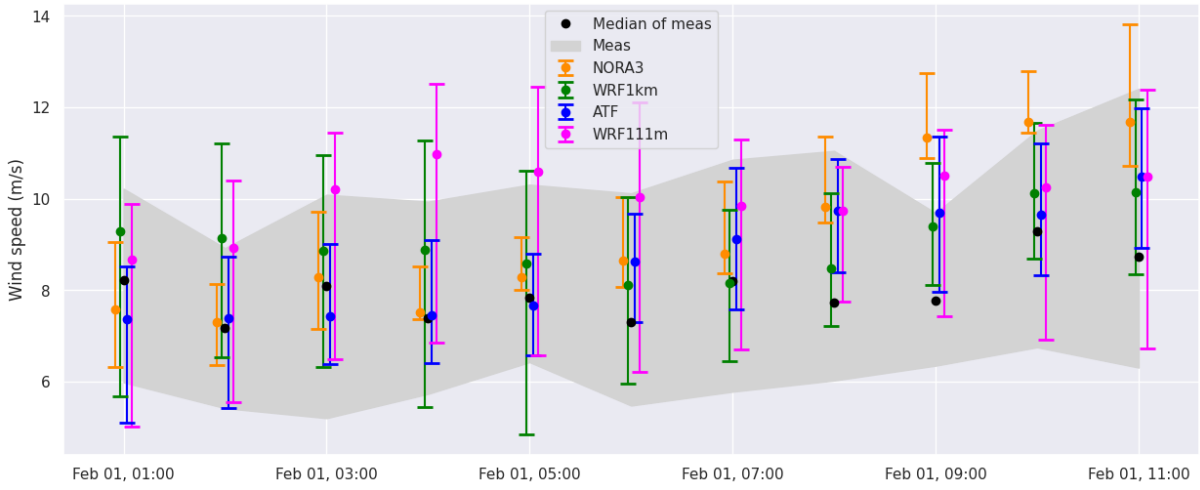

***Figure 4-18**: The sample space between the 10th and the 90th percentile of the winds speeds from the measurements (grey), NORA3 (orange), WRF1km (green), ATF300m (blue) and WRF111m (pink). The dots represent the medians.*

The averaged statistical scores of the wind speed of all turbine positions for each model are represented in Table 4-6. The lowest averaged MAE, MBE and RMSE are found for ATF300m. This was also seen in section 4.1 where ATF300m outperformed the other models during the 9 months period. This suggests that ATF300m is the model performing the best at conditions occurring most frequently. Contrary to the January case, NORA3 now performs the worst out of all models with the highest MAE and RMSE scores. The bad performance is possibly due to poor topography representation leading to a lack of orographic effects on the air flow.

***Table 4-6**: The averaged MAE, MBE and RMSE of the wind speed of all turbine positions for each model*

Model	MAE	MBE	RMSE
NORA3	2.01	1.33	2.38
WRF1km	1.39	0.84	1.65
ATF300m	1.33	0.52	1.58
WRF111m	1.76	1.46	2.05

The largest variance in the wind speed measurements is found at 11:00 UTC and this particular time is therefore further studied. The spatial distribution of power production and the model's power biases at 11:00 UTC are shown in Figure 4-19. All models show a tendency of overestimating the power production, except at the northernmost locations where the power production is well reproduced.

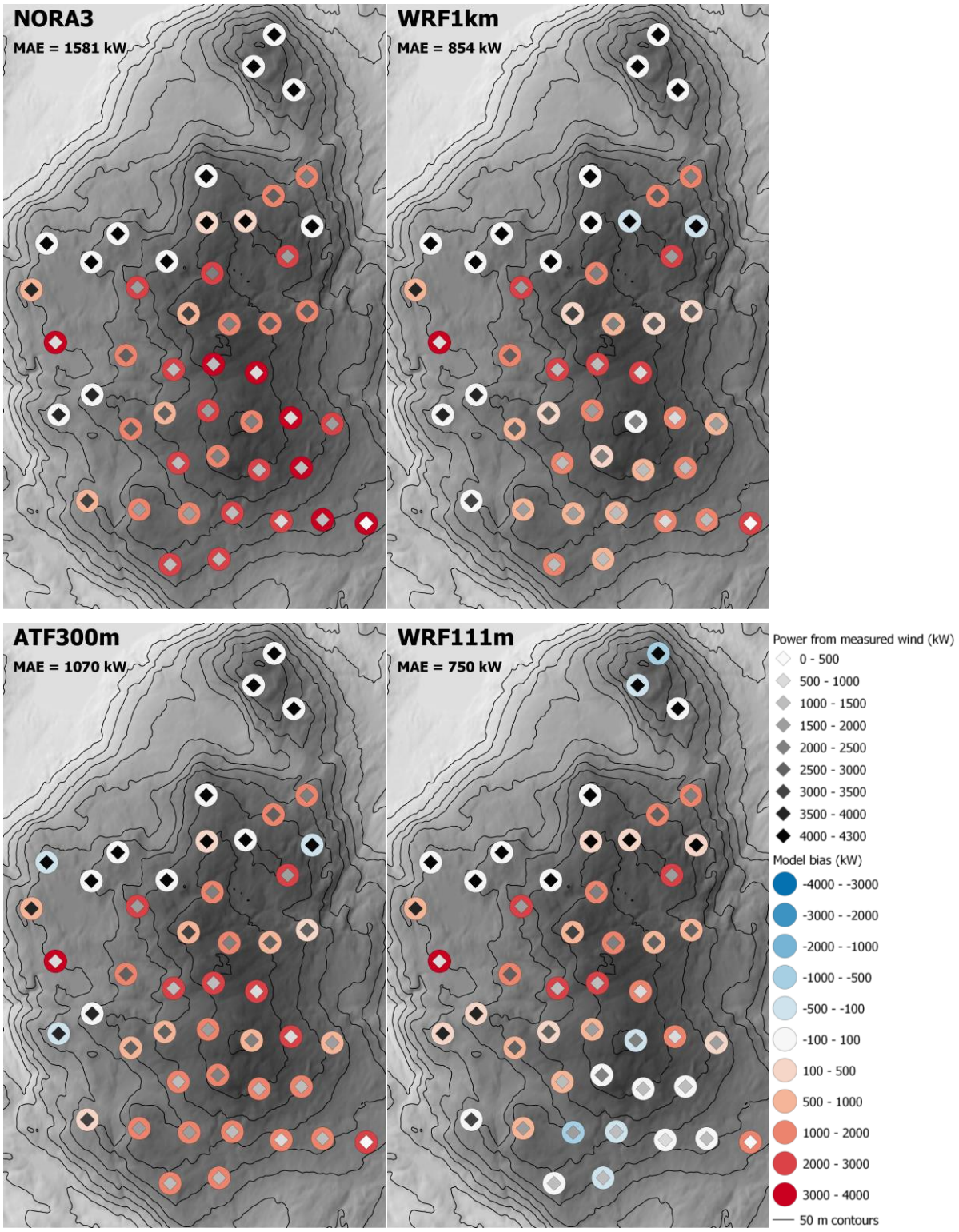

***Figure 4-19**: The spatial distribution of the models' power biases on February 1st 11:00 UTC.*

NORA3 (top left) is the model with the largest overestimation of power production in the upwind area southeast in the park, which could explain the high MAE value of the model. The differences between WRF1km (top right) and ATF300m (bottom left) are found south in the park where WRF1km outperforms ATF300m by reproducing the power production closer to

the measurements. WRF111m (bottom right) is the model with the lowest MAE at the investigated time which may be related to how well WRF111m reproduces the power production southeast in the park, where all other models tend to overestimate. This is the area in the power plant where the power production is the lowest. Towards the middle of the farm, the overestimation by the model increases, indicating that WRF111m overshoots the measured wind speeds at these locations.

The measured and modelled wind speeds and directions are shown in Figure 4-20 at the same instant moment. The MAE in the upper left corner of each panel represents the spatial averaged absolute error of the wind speeds. The measured wind direction represented by the white arrows is coming from S-SE at most turbine locations. However, five locations stand out where the measured wind direction is E or NE. The modelled wind direction represented by the colored arrows are failing to reproduce the deviating wind direction measured at these locations for all models. However, by examining the previous and the following wind direction measurements for these turbines, one of them is measuring the wind direction to a constant value for over 24 hours. This suggests that the turbine of interest is controlled in some way and that its measurements should be ignored as they are not representative for the actual wind conditions. Interpreting the other outliers are therefore done with caution.

The models are reproducing the main S-SE wind direction well, although they all have a general tendency in producing a stronger southerly component. The models are in general agreement to where they deviate the most from the measurements, although no pattern is clear as the largest offsets are found at several distinct locations. These locations are found at the mountain top north in the park, in the middle of the park, and to the west, east and south in the park.

When considering the modelled wind speeds represented by the colored arrows it is clear that all models tend to overestimate the wind speed. The wind speeds simulated by NORA3 (upper left panel) are only separated into two classes above 10 m/s. This small variance in wind speeds is expected due to the few distinct locations resolved by NORA3. At the northernmost locations, NORA3 reproduces the wind speeds well in accordance with the measurements. Moving towards the middle and southwards in the park, the overestimation gets more prominent. This is all in agreement with the modelled power production from Figure 4-19. At two turbine positions, one located to the west in the park, the second located furthest southeast in the park,

the overestimation exceeds 6 m/s. NORA3 is the model with the highest MAE of all models, likely as a result of the strong overestimation found in the park.

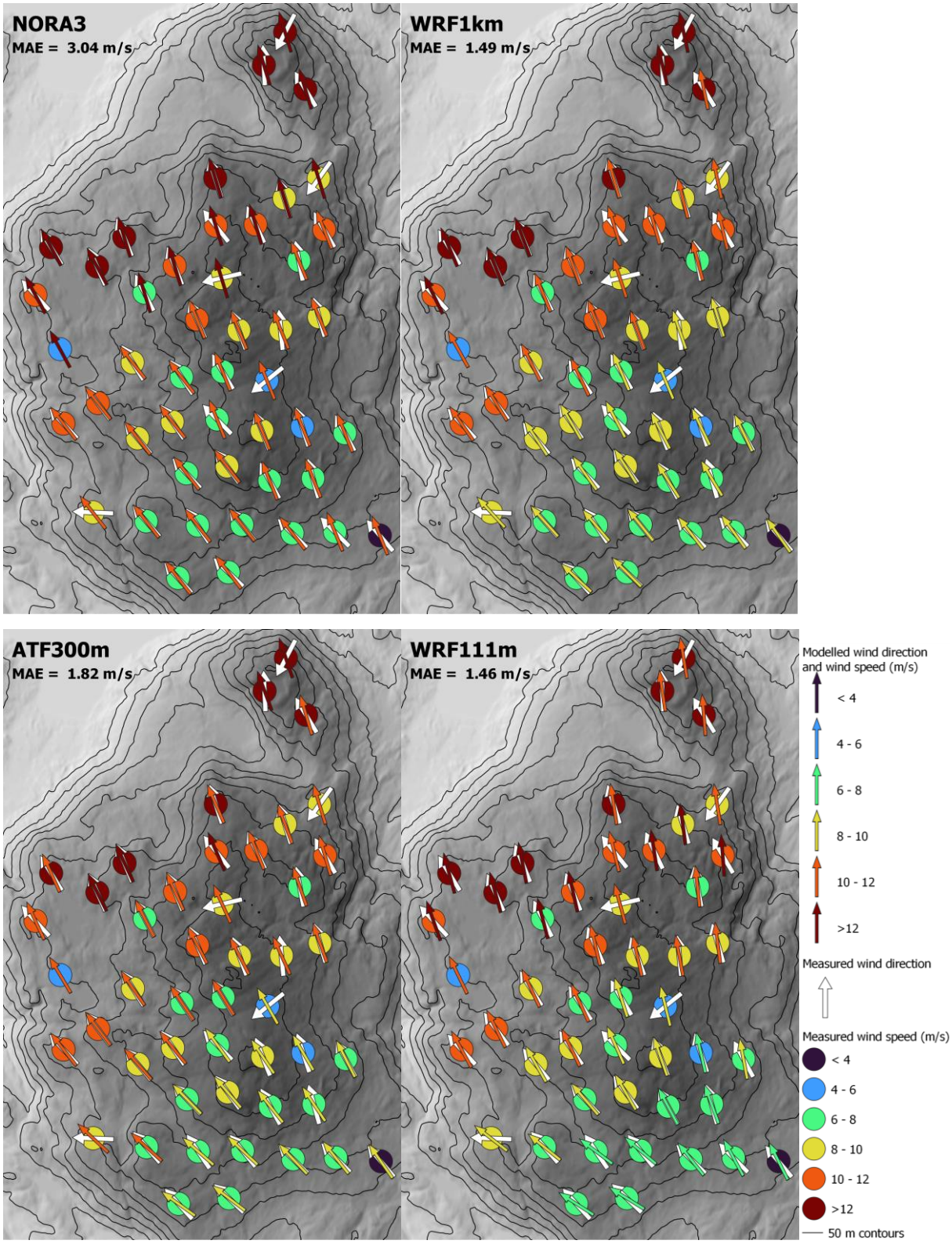

***Figure 4-20**: Measured and modelled wind speeds and directions at the 47 turbine locations on February 1st 11:00 UTC.*

WRF1km (upper right panel) scores somewhat worse than NORA3 for the northernmost locations with brown fields of measured wind speeds above 12 m/s as the model underestimates the wind speeds at some of these locations. However, for the locations near the middle where the measurements show yellow and orange fields of wind speeds of 8 to 12 m/s, WRF1km reproduces the wind speeds well. This may explain why WRF1km has the second lowest MAE value. At the southernmost locations, the model overestimates the wind speeds, although not to the same extent as NORA3.

ATF300m (bottom left panel) overestimates the wind speeds in a higher degree compared to WRF1km, although still well below the degree of NORA3. The model reproduces the wind speeds best for locations further north and west in the park where the measurements show orange and brown fields of wind speeds above 10 m/s. For wind speeds below 10 m/s, the overestimation is more prominent.

WRF111m (bottom right panel) is the model with the overall lowest MAE of all models, marginally better than WRF1km. WRF111m is the only model that reproduces the green fields of measured wind speeds of 6-8 m/s located in the south. This could be explained by WRF111m's better ability to resolve the terrain where all heights, including the ones located southeast of Kvitfjell, are more detailed as discussed in section 4.3.1 (see Figure 4-13). As the wind blows from the southeast, these heights could have slowed the wind down or partially blocked it on its way towards Kvitfjell. As the models with coarser horizontal resolution either resolve the heights less accurate or are completely missing the heights, the modelled wind may flow more unaffected resulting in higher wind speeds at the upwind side of Kvitfjell. Some of the fields of measured wind speeds above 8 m/s located near the middle and further west in the park are also well reproduced by WRF111m, while the model deviates more from the measurements at locations east and north in the park. At the mountain top northeast in the park, WRF111m is the only model underestimating the wind speeds at all three turbine positions.

4.3.4 May 2022

The wind measurements from May 15th 15:00 UTC until May 16th 15:00 UTC are represented by the wind rose in Figure 4-21. The main wind direction during this period is 315°-0° (NW-N). This particular direction is just the opposite of the main wind direction for the 9-month period. The wind speeds mostly range between 6 to 12 m/s.

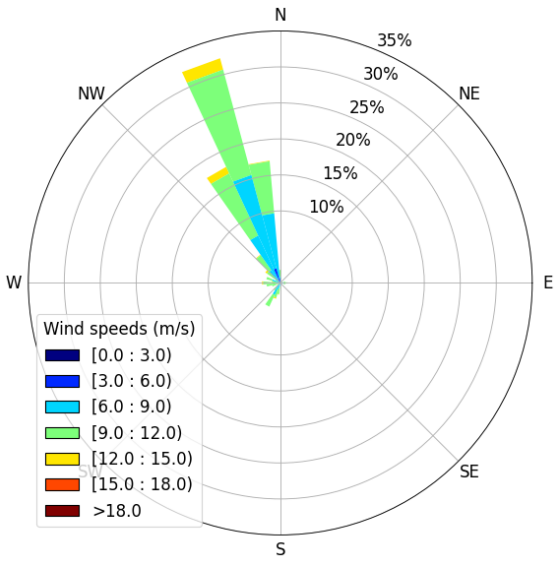

***Figure 4-21**: Windrose for the combined hourly measurements of all 47 turbines between May 15th 15:00 UTC and May 16th 15:00 UTC.*

The sample spaces between the 10th and the 90th percentile of the measured and simulated wind speeds are shown in Figure 4-22. All models are overestimating the wind speeds throughout the 24 hours simulation period, except of a few models underestimating at three hours. Most prominent is the continuously overestimating by all models from May 15, 20:00 UTC until May 16, 04:00 UTC. WRF111m stands out as the model with the largest overestimation at most hours.

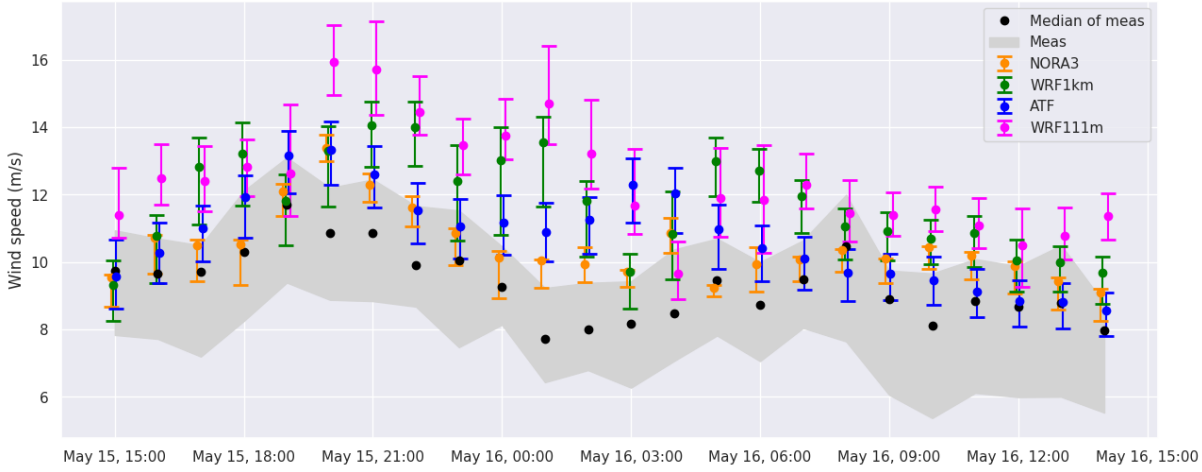

***Figure 4-22:** The sample space between the 10th and the 90th percentile of the winds speeds from the measurements (grey), NORA3 (orange), WRF1km (green), ATF300m (blue) and WRF111m (pink). The dots represent the medians.*

The averaged MAE, MBE and RMSE of the wind speeds of all turbine positions for each model are represented in Table 4-7. NORA3 outperforms the other models with the lowest averaged statistical scores as for the January case. The wind directions for both this and the January case

were in the NW sector (270°-360°) which may indicate that NORA3 performs well during conditions where the wind mainly comes from the open sea and is unaffected by any topography. However, it is also possible that one error related to the model may counteract the effect from another, yielding good reproduction of the wind speed. These cancelling factors could for instance be the coarse spatial resolution of NORA3 counteracting the missing wind farm parameterization. As NORA3 simulates low variance in wind speeds often with lower magnitude than the finer models (Figure 4-15 and Figure 4-22), the overestimation caused by ignoring wind farm effects would be less evident.

***Table 4-7**: The averaged statistical scores of the wind speed for each model.*

Model	MAE	MBE	RMSE
NORA3	1.59	1.17	1.85
WRF1km	2.68	2.38	3.04
ATF300m	1.92	1.50	2.25
WRF111m	3.42	3.36	3.82

The largest variance in wind speed measurements is found at May 16, 13:00 UTC. The spatial distributed power biases of the models are shown in Figure 4-23. All models overestimate the power production at turbine locations south in the park. Of all the models, WRF111m has the highest bias in this region which may be an explanation for why it has the highest MAE score. However, WRF111m reproduces well the power production at turbine locations north in the park, where the rest of the models are underestimating.

4.4 Sources of error

The measurements are affected by being recorded within a wind power plant. Wind turbine wakes lower the wind speed downwind of a wind turbine as discussed in 2.3.2. The tendency of overestimating wind speeds and thus power production observed for all models is therefore not surprising as none of the models take the turbine effects into account. If the air doesn't go back to free state before reaching the next turbine in the power plant, the wind speed is further reduced. If this was the case at Kvitfjell, one would expect the biases of the wind speed and the power production to increasingly propagate towards the lee side of the mountain. This was not observed during the 9 months study, nor for the case study of February 2022 with SE wind

direction. However, for the two other case studies during January and May 2022, the overestimation of wind speeds increased downwind in the power plant. This could be explained as a result of increased turbine wake effects downwind.

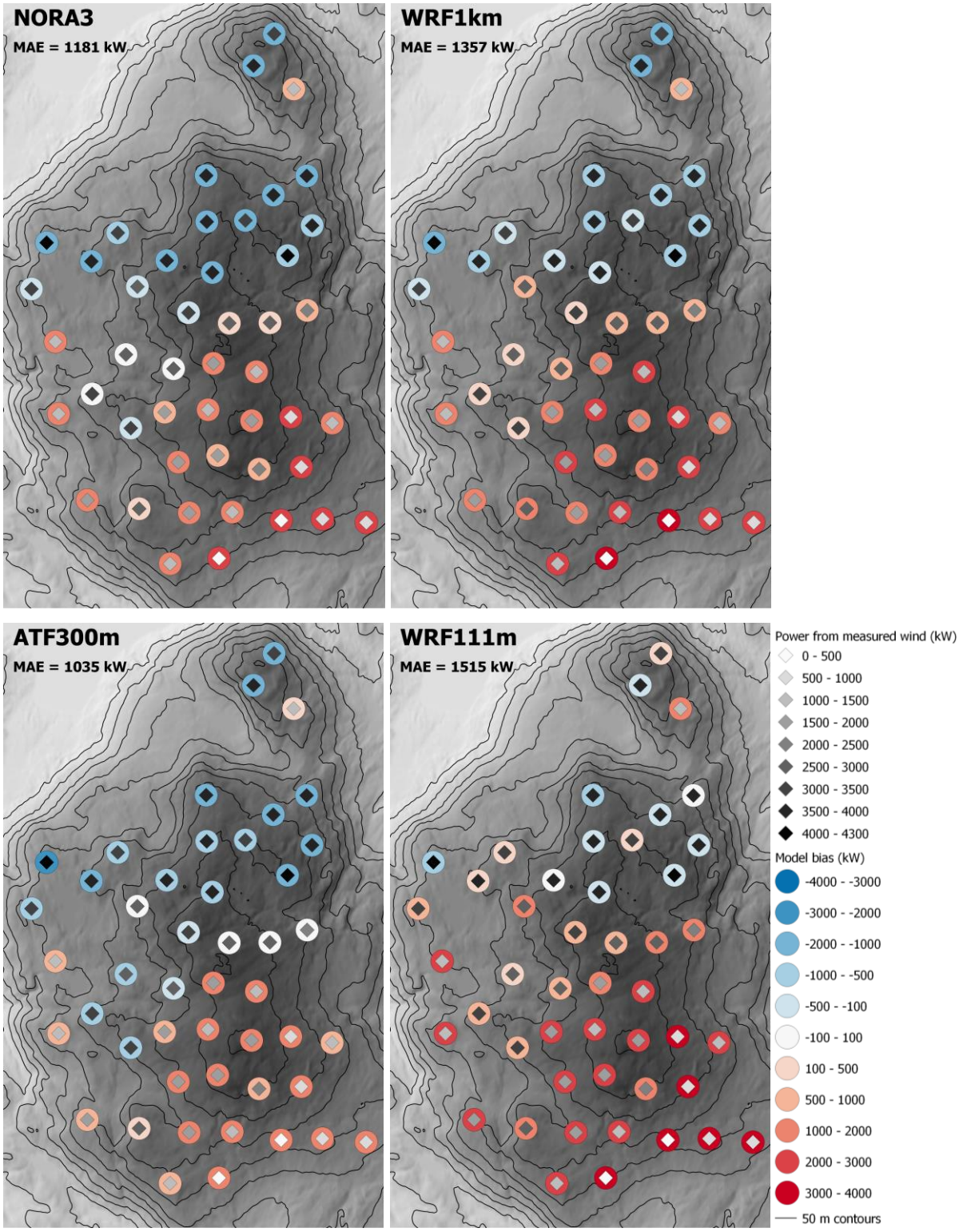

Figure 4-23: *The spatial distribution of the models' power biases on May 16th 13:00 UTC.*

The measurements are sampled every 10^{th} minute and represent the average wind speed within these 10 minutes. However, the model outputs are only snapshots of the wind at the exact moment and not averaged as the measurements. Fluctuations in the wind might have been simulated by the model during a 10 minute period, and the model output might therefore not be representable as a mean for the wind conditions during the last 10 minutes.

Only hourly data have been compared. This means that for the measurements recorded as an average every tenth minute, it is assumed that the averaged wind speed between the 50^{th} and 60^{th} minute is representable for the entire hour as the hourly energy production is found from this wind speed. For the model data, this means that the wind speed simulated at the exact hour is assumed representable for the entire hour as the modelled energy production is found based on the wind speed at each hour. This leads to uncertainties related to the accuracy of the power production found from both the wind speed measurements and the modelled wind speeds.

Different methods were used for interpolating and extracting the wind speed data for the different models due to their format differences. Not applying the same routines can introduce method related errors in the data.

The accuracy of the measured wind speed and direction may also be questionable as the discarded data only included missing measurements ("NaN"s). The measured data used for analysis could therefore still contain inaccuracies as a result of turbine maintenance, icing, testing, manually controlling or any other events influencing the measuring of either wind speed or direction. Applying procedures taking the recorded turbine error and alarm logs into account would have strengthened the reliability of the provided turbine data.

5 Conclusion

This thesis has compared how well the wind direction, the wind speed, and the associated power production at Kvitfjell wind power plant is reproduced by numerical weather models with horizontal resolutions on a hectometric and km-scale. The time period considered covered the 9 months from January through September 2022. The models used for this purpose included NORA3, WRF and ATF with horizontal resolutions at 3 km, 1 km and 300 m, respectively. The simulated wind speeds and the associated power and energy production have been compared to the hub-height measured wind speeds at 47 turbine locations. The results showed that all models overestimate the occurrence of wind speeds above 7 m/s and the associated power production and energy generation in this wind speed range. The overestimation might be a result of wind turbine wakes affecting the measurements, while all simulations are run without taking any turbine effects into account. ATF300m reproduced the wind speeds, the wind directions and the power production with the lowest averaged MAE, MBE and RMSE. This was explained by the more accurate topographic representation by ATF300m due to its higher spatial resolution compared to NORA3 and WRF1km. A better representation of the terrain can lead to increased topographic effects on the air flow such as orographic blocking.

Three cases of shorter duration with steady wind speeds and wind directions during January, February and May 2022 were further studied. For these cases, model runs from WRF with horizontal resolution of 111m were also included. For the cases of January and May, the measured wind directions were coming from the NW sector (270°-360°), mainly from open ocean leaving the wind unaffected by topography before entering Kvitfjell. Almost all models showed a tendency in overestimating the wind speeds at the downwind side of the mountain. This might be explained by the models not considering the turbine wake effects within the park. NORA3 reproduced the wind speeds most accurately in terms of yielding the lowest average scores of MAE, MBE and RMSE. This may suggest that a spatial resolution of 3 km is sufficient to reproduce the wind speeds when the wind is mostly unaffected by terrain before entering the park. Another explanation for the favorable results could be that the coarse resolution of NORA3 yields lower wind speeds making the absence of wind farm parameterization less evident.

For the February case with a main wind direction of S-SE, the models mostly overestimated the wind speeds and hence the power production. A snapshot of the spatial distribution of the power production showed that all models reproduced the power production downwind of the mountain

well, while WRF111m in addition simulated the power production in good agreement with the measurements at the upwind side of the mountain. This was explained by WRF111m's better ability to resolve the terrain SE of Kvitfjell where heights may block or sink the wind. However, ATF300m was the model yielding lowest errors in terms of averaged MAE, MBE and RMSE when considering the time period as a whole.

Considering all three cases from 2022 as a whole, WRF111m was the model overestimating the wind speeds the most with the highest MBE values. This may indicate that as the horizontal resolution is increased, higher wind speeds are simulated and thus yielding a higher overestimation. However, this is not certain as ATF300m has shown to be in the opposite scale by clearly underestimating the wind speeds for the January case (Figure 4-15).

In summary, this thesis found that the wind direction, wind speed and the associated power production are generally reproduced more accurately by using the hectometric model ATF300m compared to NORA3 and WRF1km with coarser horizontal resolutions. This is evident from the reduced scores of MAE, MBE and RMSE. The improved results may be due to the better topographic representation by ATF300m yielding stronger terrain induced effects on the wind like orographic blocking. The degree of improvement is however uncertain as running models with higher resolution increases the computational cost. Wind speed overestimation is prominent in most simulations, contrary to WRF's underestimation of high wind speeds in Carvalho et al. (2012) and Fernández-González et al. (2018). The overestimation may be due to the turbine wake effects not being considered by the numerical weather models and measures taking this into account could have improved the results.

5.1 Future research

Wind speed overestimation is characterizing the results from all models throughout the investigated period. However, none of the models studied in this thesis have considered the presence of the wind turbines. The wind conditions at Kvitfjell are undoubtedly affected by the wind power plant where wind measurements may be lowered for wind shadowed turbines located in areas intersecting with a turbine wake. Future work should therefore include the effects from the turbines in the model simulations to investigate whether the results are improved in terms of lowering the wind speed overestimation. A wind farm parameterization has been implemented in WRF where the wind farm is represented as a momentum sink and a source of electricity and turbulent kinetic energy (Fitch et al., 2012).

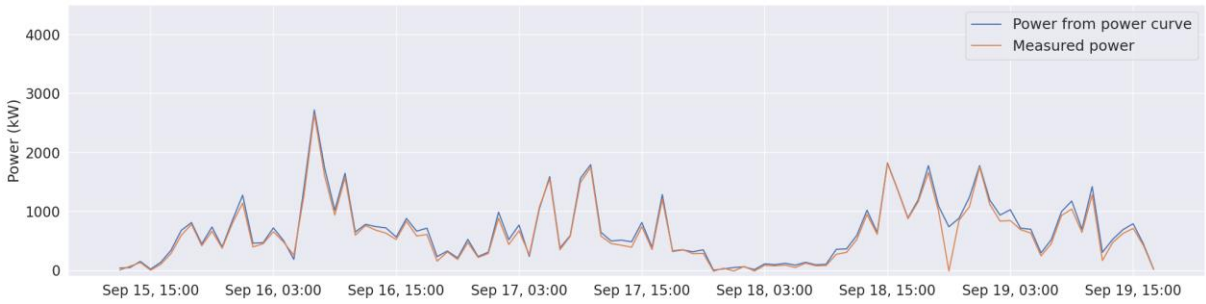

***Figure 5-1**: Fluctuations in power production observed for turbine 50 during a period in September 2022.*

While working with the data it was noted for certain locations that rapid changes in power production occurred during small time windows as represented in Figure 5-1. Such variations in power production highlights the nature of wind characterized by its intermittency and thus the challenges related to wind power trading. Another interesting topic for further investigation could therefore be to explore if any of the numerical weather models are able to capture these rapid fluctuations in power production during such small time windows.

References

Ahrens, C. D., & Henson, R. (2020). *Meteorology Today: An Introduction to Weather, Climate, and the Environment* (13 ed.). Boston: Cengage Learning, Inc.

Al-Yahyai, S., Charabi, Y., & Gastli, A. (2010). Review of the use of Numerical Weather Prediction (NWP) Models for wind energy assessment. *Renewable and Sustainable Energy Reviews, 14*(9), 3192-3198. https://doi.org/10.1016/j.rser.2010.07.001

Barthelmie, R. J., Frandsen, S. T., Rathmann, O., Hansen, K. S., Politis, E. S., Prospathopoulos, J., et al. (2008). *Flow and wakes in large wind farms in complex terrain and offshore*. Paper presented at the European Wind Energy Conference & Exhibition, Brussels. https://oa.upm.es/20943/

Battisti, L. (2015). *Wind Turbines in Cold Climates: Icing Impacts and Mitigation Systems* (2015 ed.). Cham: Cham: Springer International Publishing AG.

Bengtsson, L., Andrae, U., Aspelien, T., Batrak, Y., Calvo, J., de Rooy, W., et al. (2017). The HARMONIE–AROME Model Configuration in the ALADIN–HIRLAM NWP System. *Monthly Weather Review, 145*(5), 1919-1935. https://doi.org/10.1175/MWR-D-16-0417.1

Buvik, M., Cabrol, J., Splide, D., Skaansar, E., Roos, A., Tveten, Å. G., et al. (2022). *Norsk og nordisk effektbalanse fram mot 2030.* 94. Retrieved from https://publikasjoner.nve.no/rapport/2022/rapport2022_20.pdf

Carvalho, D., Rocha, A., Gómez-Gesteira, M., & Santos, C. (2012). A sensitivity study of the WRF model in wind simulation for an area of high wind energy. *Environmental Modelling & Software, 33*, 23-34. https://doi.org/10.1016/j.envsoft.2012.01.019

Chen, F., Kusaka, H., Bornstein, R., Ching, J., Grimmond, C. S. B., Grossman-Clarke, S., et al. (2011). The integrated WRF/urban modelling system: development, evaluation, and applications to urban environmental problems. *International Journal of Climatology, 31*(2), 273-288. https://doi.org/10.1002/joc.2158

de Rooy, W. C., & Pier Siebesma, A. (2010). Analytical expressions for entrainment and detrainment in cumulus convection. *Quarterly Journal of the Royal Meteorological Society, 136*(650), 1216-1227. https://doi.org/10.1002/qj.640

de Rooy, W. C., & Siebesma, A. P. (2008). A Simple Parameterization for Detrainment in Shallow Cumulus. *Monthly Weather Review, 136*(2), 560-576. https://doi.org/10.1175/2007MWR2201.1

Doyle, J. D., Epifanio, C. C., Persson, A., Reinecke, P. A., & Zängl, G. (2013). Mesoscale Modeling over Complex Terrain: Numerical and Predictability Perspectives. In F. K. Chow, S. F. J. De Wekker, & B. J. Snyder (Eds.), *Mountain Weather Research and Forecasting: Recent Progress and Current Challenges* (pp. 531-589). https://doi.org/10.1007/978-94-007-4098-3_9

ECMWF. (1989). *ECMWF forecast model: Physical parameterization.* ECMWF Res. Manual RM-3, pp. 154.

ECMWF. (2015). IFS Documentation CY41R1 - Part IV: Physical Processes. In *IFS Documentation CY41R1* (pp. 213). https://doi.org/10.21957/p50qmwprw

Fernández-González, S., Martín, M. L., García-Ortega, E., Merino, A., Lorenzana, J., Sánchez, J. L., et al. (2018). Sensitivity Analysis of the WRF Model: Wind-Resource Assessment for Complex Terrain. *Journal of Applied Meteorology and Climatology, 57*(3), 733-753. https://doi.org/10.1175/JAMC-D-17-0121.1

Fitch, A. C., Olson, J. B., Lundquist, J. K., Dudhia, J., Gupta, A. K., Michalakes, J., et al. (2012). Local and Mesoscale Impacts of Wind Farms as Parameterized in a Mesoscale NWP Model. *Monthly Weather Review, 140*(9), 3017-3038. https://doi.org/10.1175/MWR-D-11-00352.1

González-Longatt, F., Wall, P., & Terzija, V. (2012). Wake effect in wind farm performance: Steady-state and dynamic behavior. *Renewable Energy*, *39*(1), 329-338. https://doi.org/10.1016/j.renene.2011.08.053

Hersbach, H., Bell, B., Berrisford, P., Hirahara, S., Horányi, A., Muñoz-Sabater, J., et al. (2020). The ERA5 global reanalysis. *Quarterly Journal of the Royal Meteorological Society*, *146*(730), 1999-2049. https://doi.org/10.1002/qj.3803

Homola, M. C. (2011). *Atmospheric icing on wind turbines: Modeling and consequences for energy production.* (Degree of philosophiae doctor). Norwegian University of Science and Technology Retrieved from http://hdl.handle.net/11250/260519 NTNU Open database.

Haakenstad, H., Breivik, Ø., Furevik, B. R., Reistad, M., Bohlinger, P., & Aarnes, O. J. (2021). NORA3: A Nonhydrostatic High-Resolution Hindcast of the North Sea, the Norwegian Sea, and the Barents Sea. *Journal of Applied Meteorology and Climatology*, *60*(10), 1443-1464. https://doi.org/10.1175/JAMC-D-21-0029.1

IPCC. (2022). Summary for Policymakers. In: Climate Change 2022: Mitigation of Climate Change. Contribution of Working Group III to the Sixth Assessment Report of the Intergovernmental Panel on Climate Change [P.R. Shukla, J. Skea, R. Slade, A. Al Khourdajie, R. van Diemen, D. McCollum, M. Pathak, S. Some, P. Vyas, R. Fradera, M. Belkacemi, A. Hasija, G. Lisboa, S. Luz, J. Malley, (eds.)]. Cambridge University Press, Cambridge, UK and New York, NY, USA. doi: 10.1017/9781009157926.001.

IPCC. (2023). Summary for Policymakers. In: Climate Change 2023: Synthesis Report. A Report of the Intergovernmental Panel on Climate Change. Contribution of Working Groups I, II and III to the Sixth Assessment Report of the Intergovernmental Panel on Climate Change [Core Writing Team, H. Lee and J. Romero (eds.)]. IPCC, Geneva, Switzerland, 36 pages. (in press).

Jackson, P. L., Mayr, G., & Vosper, S. (2013). Dynamically-Driven Winds. In F. K. Chow, S. F. J. De Wekker, & B. J. Snyder (Eds.), *Mountain Weather Research and Forecasting: Recent Progress and Current Challenges* (pp. 121-218). Dordrecht: Springer Netherlands.

Jiménez, P. A., & Dudhia, J. (2013). On the Ability of the WRF Model to Reproduce the Surface Wind Direction over Complex Terrain. *Journal of Applied Meteorology and Climatology*, *52*(7), 1610-1617. Retrieved from http://www.jstor.org/stable/26175853

Jiménez, P. A., Dudhia, J., González-Rouco, J. F., Navarro, J., Montávez, J. P., & García-Bustamante, E. (2012). A Revised Scheme for the WRF Surface Layer Formulation. *Monthly Weather Review*, *140*(3), 898-918. https://doi.org/10.1175/mwr-d-11-00056.1

Kain, J. S. (2004). The Kain–Fritsch Convective Parameterization: An Update. *Journal of Applied Meteorology*, *43*(1), 170-181. https://doi.org/10.1175/1520-0450(2004)043<0170:TKCPAU>2.0.CO;2

Khairoutdinov, M., & Kogan, Y. (2000). A New Cloud Physics Parameterization in a Large-Eddy Simulation Model of Marine Stratocumulus. *Monthly Weather Review*, *128*(1), 229-243. https://doi.org/10.1175/1520-0493(2000)128<0229:ANCPPI>2.0.CO;2

Lascaux, F., Richard, E., & Pinty, J.-P. (2006). Numerical simulations of three different MAP IOPs and the associated microphysical processes. *Quarterly Journal of the Royal Meteorological Society*, *132*(619), 1907-1926. https://doi.org/10.1256/qj.05.197

Leite, G. d. N. P., Araújo, A. M., & Rosas, P. A. C. (2018). Prognostic techniques applied to maintenance of wind turbines: a concise and specific review. *Renewable and Sustainable Energy Reviews*, *81*, 1917-1925. https://doi.org/10.1016/j.rser.2017.06.002

Lenderink, G., & Holtslag, A. A. M. (2004). An updated length-scale formulation for turbulent mixing in clear and cloudy boundary layers. *Quarterly Journal of the Royal Meteorological Society, 130*(604), 3405-3427. https://doi.org/10.1256/qj.03.117

Letcher, T., & Letcher, T. M. (2017). *Wind energy engineering : a handbook for onshore and offshore wind turbines*(1st edition. ed.).

McMurdie, W. L., & Houze, R. A. (2006). 8 - Weather Systems. In J. M. Wallace & P. V. Hobbs (Eds.), *Atmospheric Science (Second Edition)* (pp. 313-373). San Diego: Academic Press.

Mlawer, E. J., Taubman, S. J., Brown, P. D., Iacono, M. J., & Clough, S. A. (1997). Radiative transfer for inhomogeneous atmospheres: RRTM, a validated correlated-k model for the longwave. *Journal of Geophysical Research: Atmospheres, 102*(D14), 16663-16682. https://doi.org/10.1029/97JD00237

Müller, M., Homleid, M., Ivarsson, K.-I., Køltzow, M. A. Ø., Lindskog, M., Midtbø, K. H., et al. (2017). AROME-MetCoOp: A Nordic Convective-Scale Operational Weather Prediction Model. *Weather and Forecasting, 32*(2), 609-627. https://doi.org/10.1175/WAF-D-16-0099.1

Nakanishi, M., & Niino, H. (2009). Development of an Improved Turbulence Closure Model for the Atmospheric Boundary Layer. *Journal of the Meteorological Society of Japan. Ser. II, 87*(5), 895-912. https://doi.org/10.2151/jmsj.87.895

NVE. (n.d.). Kvitfjell. Retrieved December 04, 2022, from https://www.nve.no/energi/energisystem/vindkraft/utbygde-vindkraftverk/vindkraftverk/?id=10414

Olje- og energidepartementet. (2022). Kraftmarkedet. Retrieved May 30, 2023, from https://energifaktanorge.no/norsk-energiforsyning/kraftmarkedet/

Olson, J. B., Kenyon, J. S., Angevine, W. A., Brown, J. M., Pagowski, M., & Sušelj, K. (2019). A Description of the MYNN-EDMF Scheme and the Coupling to Other Components in WRF–ARW. https://doi.org/10.25923/n9wm-be49

Owens, R. G., & Hewson, T. D. (2018). ECMWF User Guide. https://doi.org/10.21957/m1cs7h

Parent, O., & Ilinca, A. (2011). Anti-icing and de-icing techniques for wind turbines: Critical review. *Cold Regions Science and Technology, 65*(1), 88-96. https://doi.org/10.1016/j.coldregions.2010.01.005

Ren, Z., Verma, A. S., Li, Y., Teuwen, J. J. E., & Jiang, Z. (2021). Offshore wind turbine operations and maintenance: A state-of-the-art review. *Renewable and Sustainable Energy Reviews, 144*, 110886. https://doi.org/10.1016/j.rser.2021.110886

Sanderse, B., van der Pijl, S. P., & Koren, B. (2011). Review of computational fluid dynamics for wind turbine wake aerodynamics. *Wind Energy, 14*(7), 799-819. https://doi.org/10.1002/we.458

Siebesma, A. P., Bretherton, C. S., Brown, A., Chlond, A., Cuxart, J., Duynkerke, P. G., et al. (2003). A Large Eddy Simulation Intercomparison Study of Shallow Cumulus Convection. *Journal of the Atmospheric Sciences, 60*(10), 1201-1219. https://doi.org/10.1175/1520-0469(2003)60<1201:ALESIS>2.0.CO;2

Siebesma, A. P., Soares, P. M. M., & Teixeira, J. (2007). A Combined Eddy-Diffusivity Mass-Flux Approach for the Convective Boundary Layer. *Journal of the Atmospheric Sciences, 64*(4), 1230-1248. https://doi.org/10.1175/JAS3888.1

Siemens Gamesa. (2018). Providing more predictable power output. Retrieved May 31, 2023, from https://www.siemensgamesa.com/-/media/siemensgamesa/downloads/en/products-and-services/services/asset-optimization/high-wind-ride-through-feature.pdf

Simonsen, A. H., & Brennan, K. (2022). *Vind- og produksjonsindekser for vindkraft i Norge, 2021*. 2022-001, pp. 29. NVE. Retrieved from https://www.nve.no/media/13401/mev-ws-2022-001-vind-og-produksjonsindekser-for-vindkraft-i-norge-2021.pdf

Solbakken, K., Birkelund, Y., & Samuelsen, E. M. (2021). Evaluation of surface wind using WRF in complex terrain: Atmospheric input data and grid spacing. *Environmental Modelling & Software*, *145*, 105182. https://doi.org/10.1016/j.envsoft.2021.105182

Tewari, M., Chen, F., Wang, W., Dudhia, J., LeMone, M. A., Mitchell, K., et al. (2004). Implementation and verification of the unified NOAH land surface model in the WRF model. *20th conference on weather analysis and forecasting/16th conference on numerical weather prediction*, 11-15.

Thompson, G., Field, P. R., Rasmussen, R. M., & Hall, W. D. (2008). Explicit Forecasts of Winter Precipitation Using an Improved Bulk Microphysics Scheme. Part II: Implementation of a New Snow Parameterization. *Monthly Weather Review*, *136*(12), 5095-5115. 10.1175/2008mwr2387.1

Vagner, D., Gunnerød, J., Kringstad, A., Korneliussen, R., Christiansen, L., & Hytten, L. M. (2022). *Kortsiktig Markedsanalyse 2022-27.* Retrieved from https://www.statnett.no/om-statnett/nyheter-og-pressemeldinger/nyhetsarkiv-2022/kortsiktig-markedsanalyse-okende-forbruk-gir-kraftunderskudd-fra-2027/

van Meijgaard, E., Ulft, L. H. v., Lenderink, G., Roode, S. R. d., Wipfler, L., Boers, R., et al. (2012). *Refinement and application of a regional atmospheric model for climate scenario calculations of Western Europe*. 44.

Wagner, H.-J., & Mathur, J. (2017). *Introduction to Wind Energy Systems: Basics, Technology and Operation*. Cham: Cham: Springer International Publishing AG.

Wallace, J. M., & Hobbs, P. V. (2006a). 1 - Introduction and Overview. In J. M. Wallace & P. V. Hobbs (Eds.), *Atmospheric Science (Second Edition)* (pp. 1-23). San Diego: Academic Press.

Wallace, J. M., & Hobbs, P. V. (2006b). 7 - Atmospheric Dynamics. In J. M. Wallace & P. V. Hobbs (Eds.), *Atmospheric Science (Second Edition)* (pp. 271-311). San Diego: Academic Press.

Wang, W., Bruyère, C., Duda, M., Dudhia, J., Gill, D., Kavulich, M., et al. (2017). User's Guide for the Advanced Research WRF (ARW) Modelling System, Version 3.9. Retrieved 01. November, 2022, from https://www2.mmm.ucar.edu/wrf/users/docs/user_guide_V3/user_guide_V3.9/ARWUsersGuideV3.9.pdf

Wang, X., Guo, P., & Huang, X. (2011). A Review of Wind Power Forecasting Models. *Energy Procedia*, *12*, 770-778. https://doi.org/10.1016/j.egypro.2011.10.103

Willmott, C. J., & Matsuura, K. (2005). Advantages of the mean absolute error (MAE) over the root mean square error (RMSE) in assessing average model performance. *Climate research*, *30*(1), 79-82. https://doi.org/10.3354/cr030079

Zephyr. (n.d.). Kvitfjell Raudfjell. Retrieved May 19, 2022, from https://zephyr.no/portfolio/kvitfjell-raudfjell-vindkraftverk/

Appendix A: WRF namelist.input

```
&time_control
run_days                 = 0,
run_hours                = 20,
run_minutes              = 00,
run_seconds              = 00,
start_year               = 2022, 2022, 2022, 2022 ,2020,
start_month              = 01, 01, 01, 01, 12,
start_day                = 13, 13, 13, 13, 26,
start_hour               = 12, 12, 12, 12, 00, 00,
start_minute             = 00, 00, 00, 00, 00, 00,
start_second             = 00, 00, 00, 00, 00, 00,
end_year                 = 2022, 2022, 2022, 2022, 2020,
end_month                = 01, 01, 01, 01, 12,
end_day                  = 14, 14, 14, 14,
end_hour                 = 08, 08, 08, 08, 00, 00,
end_minute               = 00, 00, 00, 00, 00, 00,
end_second               = 00, 00, 00, 00, 00, 00,
interval_seconds         = 3600,
input_from_file          = .true., .true., .true., .true., .true., .true.,
history_interval         = 10, 10, 10, 10, 10, 10,
frames_per_outfile       = 36, 36, 36, 36, 1000, 1000
restart                  = .false.,
restart_interval         = 1440,
io_form_history          = 2,
io_form_restart          = 2,
io_form_input            = 2,
io_form_boundary         = 2,
debug_level              = 0,
/

&domains
time_step                = 30,
time_step_fract_num      = 0,
time_step_fract_den      = 1,
max_dom                  = 4,
e_we                     = 100,      100,      100, 109, 604,
e_sn                     = 100,      100,      100, 118, 406,
e_vert                   = 70,       70,       70,  70,  70,
p_top_requested          = 5000,
num_metgrid_levels       = 38,
num_metgrid_soil_levels  = 4,
dx                       = 9000,     3000,   1000,  111.111, 10.10101,
dy                       = 9000,     3000,   1000,  111.111, 10.10101,
grid_id                  = 1,        2,      3,     4,       5,
parent_id                = 1,        1,      2,     3,       4,
i_parent_start           = 1,        30,     43,    54,      31,
j_parent_start           = 1,        32,     35,    58,      51,
parent_grid_ratio        = 1,        3,      3,     9,       9,
parent_time_step_ratio   = 1,        3,      3,     9,       9,
feedback                 = 0,
smooth_option            = 0,
smooth_cg_topo           = .true.,
/
```

```
&physics
mp_physics                = 8, 8, 8,8,8,
ra_lw_physics             = 4, 4,      4, 4, 4,
ra_sw_physics             = 4, 4,      4, 4, 4,
sf_sfclay_physics         = 1, 1,      1, 1, 1,
sf_surface_physics        = 2, 2,      2, 2, 2,
bl_pbl_physics            = 5, 5,      5, 0, 0,
cu_physics                = 1, 1,      1, 0, 0,
radt                      = 10, 10,     10, 10, 10,
bldt                      = 0, 0,      0, 0, 0,
cudt                      = 5, 5,      5, 5, 5,
isfflx                    = 1,
icloud                    = 1,
surface_input_source      = 1,
num_soil_layers           = 4,
sf_urban_physics          = 1, 1, 1, 1, 1,
/

&fdda
/

&dynamics
w_damping                 = 1,
diff_opt                  = 2, 2, 2, 1,
km_opt                    = 4, 4, 4, 3,
smdiv                     = 0.1, 0.1, 0.1, 0.1,
emdiv                     = 0.01, 0.01, 0.01, 0.01,
epssm                     = 0.1, 0.1,     0.1, 0.8,
diff_6th_opt              = 0, 0,       0, 0, 0,
diff_6th_factor           = 0.12,     0.12,    0.12, 0.12,
base_temp                 = 290.,
damp_opt                  = 0,
zdamp                     = 5000.,  5000.,   5000., 5000.,
dampcoef                  = 0.2,    0.2,     0.2, 0.2,
khdif                     = 0,      0,       0, 0,
kvdif                     = 0,      0,       0, 0,
non_hydrostatic           = .true., .true.,  .true., .true.,
moist_adv_opt             = 1,       1,       1, 1,
scalar_adv_opt            = 1,       1,       1, 1,
/

&bdy_control
spec_bdy_width            = 5,
spec_zone                 = 1,
relax_zone                = 4,
specified                 = .true,    .false.,  .false., .false., .false.,
nested                    = .false.,   .true.,   .true., .true., .true.,
/

&grib2
/

&namelist_quilt
nio_tasks_per_group       = 0,
nio_groups                = 1,
/

```

Appendix B: Turbine locations at Kvitfjell

Turbine number	Easting	Northing	Longitude	Latitude
	UTM (north)-WGS84 Zone: 33			
K1	622 437	7 722 561	18.14607	69.58334
K10	621 807	7 723 520	18.13117	69.59222
K11	620 867	7 723 893	18.10754	69.59599
K12	622 036	7 722 522	18.13573	69.58318
K13	622 258	7 724 830	18.14447	69.60374
K14	622 654	7 724 519	18.15423	69.60077
K15	622 599	7 725 026	18.15349	69.60534
K16	621 972	7 724 571	18.13679	69.60155
K17	622 604	7 723 650	18.15179	69.59302
K18	619 939	7 724 343	18.08431	69.60044
K19	621 168	7 724 160	18.11561	69.59824
K2	622 860	7 722 499	18.15683	69.58259
K20	621 577	7 724 557	18.12663	69.60161
K21	621 146	7 722 609	18.11302	69.58437
K22-1	620 029	7 723 331	18.08530	69.59134
K23	622 085	7 723 023	18.13765	69.58764
K24	620 750	7 723 199	18.10363	69.58983
K25	621 634	7 724 038	18.12741	69.59694
K26	621 590	7 722 635	18.12444	69.58439
K27	620 397	7 724 152	18.09581	69.59852
K28	621 689	7 722 168	18.12637	69.58017
K29	622 467	7 725 914	18.15127	69.61335
K3	622 223	7 723 525	18.14185	69.59207
K30	621 571	7 725 029	18.12710	69.60584
K31	621 397	7 721 580	18.11811	69.57504
K32	620 667	7 724 443	18.10312	69.60101
K33	622 266	7 726 479	18.14686	69.61850
K34	621 202	7 721 060	18.11243	69.57047
K35	622 112	7 722 027	18.13703	69.57871
K36	620 062	7 722 592	18.08519	69.58471
K37	619 784	7 723 869	18.07971	69.59627
K38	621 237	7 723 054	18.11593	69.58831
K39	622 338	7 721 504	18.14213	69.57392
K4	621 645	7 723 109	18.12647	69.58861
K40	620 355	7 721 711	18.09156	69.57668
K42	621 286	7 722 099	18.11594	69.57973
K43	620 885	7 721 623	18.10504	69.57565
K44	620 800	7 722 447	18.10393	69.58307
K45	622 544	7 722 049	18.14813	69.57871
K47	622 404	7 724 211	18.14740	69.59813
K48	621 838	7 721 587	18.12942	69.57490
K49	622 761	7 721 517	18.15299	69.57385

K5	621 702	7 721 116	18.12532	69.57074
K50	623 208	7 721 481	18.16441	69.57332
K6	621 390	7 723 627	18.12061	69.59337
K8	622 055	7 726 153	18.14101	69.61568
K9	620 405	7 722 796	18.09426	69.58638